Study of the vortex structure in compressible wall-bounded turbulence

Tianyi Bai [1], Cheng Cheng [1], Kevin P. Griffin [2], Xinliang Li [3] and Lin Fu [1,4,5,6,*]

[1]*Department of Mechanical and Aerospace Engineering, The Hong Kong University of Science and Technology, Clear Water Bay, Kowloon, Hong Kong*

[2]*Center for Turbulence Research, Stanford University, Stanford, California 94305, USA*

[3]*LHD, Institute of Mechanics, Chinese Academy of Sciences, Beijing 100190, China*

[4]*Department of Mathematics, The Hong Kong University of Science and Technology, Clear Water Bay, Kowloon, Hong Kong*

[5]*HKUST Shenzhen-Hong Kong Collaborative Innovation Research Institute, Futian, Shenzhen, China*

[6]*Shenzhen Research Institute, The Hong Kong University of Science and Technology, Shenzhen, China*

(Received 25 February 2023; accepted 27 October 2023; published 6 December 2023)

The similarity of turbulent structures between compressible and incompressible wall turbulence has been well recognized through mostly visualization of instantaneous fields. However, some questions remain unclear, such as will Morkovin's hypothesis and semilocal scaling, with which many mean flow profiles collapse, also be applicable to instantaneous features of turbulence structures and why. The present work dissects features of vortical structures in compressible channel flows comprehensively to address these questions by employing the direct numerical simulations database of turbulent channel flows covering broad Mach and Reynolds numbers. Most features investigated show satisfactory agreement quantitatively with the incompressible counterparts in semilocal units, which indicates the validity of Morkovin's hypothesis based on the semilocal scaling. This observation extends Morkovin's hypothesis from standard mean flow statistics to instantaneous vortex features and suggests that the dominant mechanism governing vortex evolution remains the same as incompressible flows. Specifically, the streamwise vortex inclination angle approaches 45° as the wall-normal distance grows, which is supported by a theoretical estimation extended from incompressible flows by claiming the compressibility does not alter the vortex orientation. Regarding the size and strength of vortices, the average radius of vortices grows with the wall-normal distance, while the average strength becomes weaker. The vortex population increases with Reynolds number evidently, while it decreases marginally with Mach numbers. It is impressive that the population percentage of different types of vortices is similar to all the cases in the near-wall region. Last, a heuristic model is developed as a potential candidate for describing the topology of instantaneous vortices. In cooperation with the topological model, these statistical results could be crucial input references to reconstruct flow fields using vortex methods.

DOI: 10.1103/PhysRevFluids.8.124603

I. INTRODUCTION

Vortices have been recognized as an essential flow structure responsible for the dynamics of near-wall turbulence since the early 1950s. Theodorsen [1] first and Willmarth and Tu [2], Offen and Kline [3], Perry and Chong [4], Robinson [5], and Smith *et al.* [6] subsequently propose the symmetric hairpin vortex conceptual model including leg, neck, and head in incompressible

*Corresponding author: linfu@ust.hk

turbulent boundary layers. Due to the random, chaotic, and complex nature of turbulence, as well as the sheared background of wall-bounded turbulence, asymmetric and quasistreamwise hairpins are expected and observed in the analysis of direct numerical simulations (DNS) of incompressible turbulent boundary layers and channel flows with low Reynolds number [7–9]. This conceptual model is considered. responsible for turbulence motions. The origin of many prominent features, such as streaks, ejections, and sweeps, which remains controversial for years, can be illustrated by it. Extensive studies [8–16] have been conducted. Smith *et al.* [6], and Green [17] review earlier studies and claim that central features and the observed and measured behavior of the near-wall turbulence can be elucidated by coupled interactions of hairpin vortices with each other, with the background sheared flow, and with the near-wall flow.

The statistical investigation of vortices, such as the vortex orientation, strength, size, and population, has been well explored in incompressible flows. Carlier and Stanislas [18] carry out experiments in the wind tunnel in a range of Reynolds numbers $7500 \leqslant \mathrm{Re}_\theta \leqslant 19\,000$. In the logarithmic region, eddy structures have a cane shape, which elongates downstream at an angle of 45°. Their mean radius r^+ (superscript + denoting the wall unit) increases from around 20 to around 24 with increasing wall-normal distance. In contrast, the mean vorticity decreases, which leads to an almost constant circulation $\Gamma^+ \approx 235$–250 [19]. Gao *et al.* [20] analyze the experimental and DNS data in the range of the near-wall region and report that the most probable inclination angle of vortex cores grows from 25° to 50° as the wall-normal distance increases. The radius of eddies extends from 13.7 to 14.6 for the DNS data and 14.7 ($y^+ = 110$) for the PIV data, but the mean circulation shrinks from 175 to 115 with the increasing wall-normal distance. They also examine the convection velocity of vortex cores, which is around 96%–98% of the local mean velocity. Wang *et al.* [21] perform a tomographic particle image velocimetry (TPIV) measurement on turbulent boundary layers and the DNS database at similar Reynolds numbers. Typical vortex structures are found in the instantaneous velocity field obtained by TPIV and their inclination angle increases up to 45° or −135° with the increase of the wall-normal distance. As for the vortex population, Wu and Christensen [22] investigate the number density of prograde and retrograde spanwise vortices in channel flows and boundary layers at various Re_τ. They report that prograde vortices appear more frequently near the inner edge of the logarithmic region, while retrograde vortices are predominant at the outer edge. Both inner- and outer-scaled number densities display an obvious dependence on the Reynolds number, which can be eliminated by a power law of Re_τ.

As for the vortex in compressible flows, Pirozzoli *et al.* [19] perform the DNS of a canonical supersonic turbulent boundary layer at $\mathrm{Ma} = 2$, $\mathrm{Re}_\theta = 950$ and characterize the vortex structures by their size and orientation quantitatively for the first time. Their study shows that the most probable inclination angle is around 33° in the buffer layer and 40° in the outer layer. The radius of vortex structures grows with wall-normal distance and levels off in the outer layer, attaining five to six local dissipative length scales and their circulation ($\Gamma^+ \approx 180$) does not vary significantly with the distance from the wall. The number of both spanwise and streamwise vortices decays with increasing wall-normal distance in the outer region ($y^+ > 40$). Elsinga *et al.* [23] provide a quantitative visualization of vortex structures in a supersonic turbulent boundary layer at $\mathrm{Ma} = 2.1$ and support the existence of hairpin vortex in compressible flows. Wang and Lu [24] also conduct DNSs of the compressible turbulent boundary layer at a similar Mach number and Reynolds number. They show that both hairpinlike and canelike vortices exist. The streamwise and spanwise length scales indicated by the two-point correlation of the fluctuating streamwise velocity increase with the wall-normal distance from $y^+ = 50$ to the boundary layer thickness δ, but the streamwise length scale is almost unchanged for $y^+ < 50$. The inclination angle defined as $\theta_{xy} = \arctan(\omega_y/\omega_x)$, where ω_i is the most probable vorticity component, grows from 31° in the viscous sublayer to 45° in the buffer layer and then decreases to 39° in the wake region. In the studies by Pirozzoli *et al.* [19], Elsinga *et al.* [23], and Wang and Lu [24], the vortical structures in the compressible flows show some similarities with the incompressible case. The DNS databases of compressible turbulent channel flow at $\mathrm{Ma}_b = 0.8$, 2, and 3 with $\mathrm{Re}_b = 3000$ are considered by Yao and Hussain [25], and

they observe that, with the increase of Mach number, the vortex structures become sparse and more elongated due to the stronger shear.

While the vortex structure has been extensively explored in incompressible wall-bounded turbulent flows, much less is understood as for its counterpart in compressible flows. Although the similarity of turbulent structures between compressible and incompressible flows has been established for decades by qualitative description and visualization, to what extent the similarity could be is still obscure. A quantitative comparison of the statistical characteristics, such as the vortex orientation, size, strength, and population, is necessary to demonstrate the Reynolds- and Mach-number dependence. To achieve a satisfactory agreement on these features, Morkovin's hypothesis [26] and its derivative, the semilocal scaling, might be an effective tool. Morkovin's hypothesis [26] asserts that the compressibility effects can be accounted for by the variation of mean flow properties, which has been verified for many mean statistics like mean profiles of thermodynamic properties, correlation functions, and profiles of the Reynolds stress. Many works also adopt it to develop velocity transformations [27–30] to recover the logarithmic law in compressible wall-bounded turbulence. However, the problem of whether it works for instantaneous features of vortex structures remains unclear, since the existing studies still use the viscous scales to characterize them, as summarized in the paragraph above. Furthermore, most proceeding works concentrate on a specific Mach number, i.e., the works by Pirozzoli *et al.* [19], Elsinga *et al.* [23], and Wang and Lu [24] focus on the Mach number around 2. Since these works apply various vortex identification criteria and approaches to characterize these features, they can hardly clarify the detailed Mach number effects on the statistical characteristics of the vortex structures in wall-bounded turbulence. Therefore, the present study is motivated to expose the dependence of structure similarity on Mach and Reynolds numbers and further identify the appropriate scaling for a decent agreement by systematically investigating the statistical features of vortices. It could help enhance the understanding of the flow physics of compressible wall-bounded turbulence and the future development of high-fidelity scale-resolving prediction technologies, e.g., the wall-modeled large-eddy simulation [31,32]. Meanwhile, these statistical results presenting vortex size, strength, and population, together with the topological model, provide a reliable reference for the input parameters when one intends to reconstruct the flow fields from a superposition of multiscale vortices.

The rest of this paper is organized as follows. Both the compressible and incompressible DNS databases adopted are described in Sec. II. Section III introduces the method to identify vortex structures and cores. The main results and discussions are presented in Sec. IV, including visualized vortices, the vortex orientation, the size and strength of vortex cores, the number density of vortices, and a heuristic model for the topology of vortices. Conclusion remarks are given in Sec. V.

II. DNS DATABASES AND TERMINOLOGY INTERPRETATIONS

This work employs DNS databases of compressible turbulent channel flows with different Mach and Reynolds numbers. In the following work, x denotes the streamwise direction, y the wall-normal direction, and z the spanwise direction. The computational domain is $L_x \times L_y \times L_z$, where domain lengths in the x, y, and z directions are indicated by L_x, L_y, and L_z, respectively, and h is one-half of the channel height. Parameters of the DNS setting are summarized in Table I. In order to explore the consistency with incompressible flows, two DNS cases for incompressible channel flows with $\mathrm{Re}_\tau = 547$ (M00R10K, denoted by - - - - -) in Ref. [33] and $\mathrm{Re}_\tau = 934$ (M00R19K, denoted by .....) in Ref. [34] are also considered. These two cases are carefully chosen, as their friction Reynolds numbers are close to those of present compressible flows. Detailed descriptions of the computational setups and validations of the compressible database are given in Appendix A.

Throughout this paper, both the Reynolds ($\phi = \overline{\phi} + \phi'$) and Favre ($\phi = \widetilde{\phi} + \phi''$) decompositions are utilized, where $\overline{\phi}$ and ϕ' denote the Reynolds-averaged quantity and the corresponding fluctuation, respectively, and $\widetilde{\phi} = \overline{\rho\phi}/\overline{\rho}$ and ϕ'' denote those of the Favre decomposition. The superscript $+$ indicates a nondimensionalization by the wall units, including the friction velocity $u_\tau = \sqrt{\tau_w/\overline{\rho}_w}$, the viscous length scale $\delta_\tau = \overline{\mu}_w/(u_\tau \overline{\rho}_w)$, and the density ρ_w and viscosity μ_w evaluated at the

TABLE I. The numerical parameter setting for DNS of channel flows adopted in this paper. $\mathrm{Ma}_b = u_b/c_w$ is the bulk Mach number, where u_b is the bulk velocity. $\mathrm{Re}_b = \rho_b u_b h/\mu_w$ is the bulk Reynolds number; Re_τ the friction Reynolds number; Re^*_τ the semilocal Reynolds number at $y = h$. $\triangle x^+$, $\triangle z^+$, and $\triangle y^+_w$ ($\triangle y^+_c$) denote the grid spacing in the x, z, and y directions, and the subscript w and c denote the positions near the wall and at the centerline of the channel, respectively. The color and line style shown in the last row are used to distinguish different cases.

Case	M08R3K	M08R8K	M08R17K	M15R3K	M15R9K	M15R20K	M40R5K
Re_b	3000	7667	17000	3000	9400	20020	5000
Re_τ	193	440	883	223	595	1152	574
Re^*_τ	168	381	778	148	392	770	121
Ma_b	0.8	0.8	0.8	1.5	1.5	1.5	4
L_x	$4\pi h$	$4\pi h$	$4\pi h$	$4\pi h$	$4\pi h$	$4\pi h$	$6\pi h$
L_y	$2h$	$2h$	$2h$	$2h$	$2h$	$2h$	$2h$
L_z	$2\pi h$	$2\pi h$	$2\pi h$	$2\pi h$	$2\pi h$	$2\pi h$	$2\pi h$
$\triangle x^+$	9.0	10.8	10.8	11.0	7.3	9.3	5.3
$\triangle z^+$	4.5	6.9	6.5	7.3	3.7	4.7	3.5
$\triangle y^+_w$	0.43	0.44	0.63	0.34	0.50	0.49	0.23
$\triangle y^+_c$	4.47	5.41	6.41	2.17	5.93	6.90	2.11
Label							

wall, where $\tau_w = \overline{\mu}_w(\partial\widetilde{u}/\partial y)|_w$ is the wall shear stress. For instance, $\widetilde{u}^+ = \widetilde{u}/u_\tau$, $y^+ = y/\delta_v$, $\overline{\mu}^+ = \overline{\mu}/\overline{\mu}_w$, and $\overline{\rho}^+ = \overline{\rho}/\overline{\rho}_w$. The friction Reynolds number is defined as $\mathrm{Re}_\tau = \rho_w u_\tau h/\mu_w$. The superscript * denotes a nondimensionalization by the semilocal scaling, e.g., $u^*_\tau = \sqrt{\tau_w/\overline{\rho}}$ indicates the semilocal velocity scale and $\delta^*_\tau = \overline{\mu}/(u^*_\tau\overline{\rho})$ the semilocal length scale. The semilocal Reynolds number at $y = h$ is given by $\mathrm{Re}^*_{\tau c} = \rho_c\sqrt{\tau_w/\rho_c}h/\mu_c$, where ρ_c is the density and μ_c is the dynamic viscosity at the center line. To clarify the near-wall regions, we define the region of $5 < y^* < 30$ as the buffer layer and of $y^* > 30$ and $y/h < 0.3$ as the logarithmic region.

III. VORTEX CORE IDENTIFICATION AND STATISTICAL TECHNIQUE

A number of vortex extraction methods [35–39] have been developed, which are reviewed comprehensively by Epps [40]. More recently, Wang *et al.* [41] propose an integrative algorithm for visualizing and quantifying vortices. In this work, the λ_{ci} criterion [39] is employed to visualize vortex structures. To explain this technique, we define $\boldsymbol{D}$ as the velocity gradient tensor $\nabla\boldsymbol{u}$, and $\boldsymbol{D^*}$ as its traceless part ($\boldsymbol{D^*} = \boldsymbol{D} - \frac{1}{3}\nabla\cdot\boldsymbol{u}\boldsymbol{I}$). In incompressible flows, one has $\boldsymbol{D^*} = \boldsymbol{D}$. When the discriminant of the characteristic equation of $\boldsymbol{D}$ is positive, $\boldsymbol{D}$ has one real eigenvalue λ_r with the corresponding real eigenvector $\boldsymbol{v_r}$ and two complex conjugate ones $\lambda^\pm_c = \lambda_{cr} \pm \lambda_{ci}i$ with corresponding complex eigenvectors $\boldsymbol{v_{cr}} \pm \boldsymbol{v_{ci}}i$. From this definition, λ_{ci} is the imaginary part of the complex eigenvalue λ_c of $\boldsymbol{D}$. The isosurface of λ^2_{ci} is able to visualize vortex structures, following Zhou *et al.* [39].

The λ_{ci} criterion [39] is able to distinguish the rotating and stretching motion of fluids. The local stretching rate is implied by λ_r and the stretching direction by $\boldsymbol{v_r}$. The local swirling strength is quantified by λ_{ci} in the direction $\boldsymbol{v_{cr}} \times \boldsymbol{v_{ci}}$ as shown by Zhou *et al.* [39] and Lay *et al.* [42]. Therefore, this criterion is able to identify, to a large extent, the topological feature of vortices, which are described by Robinson [43] asserting that "a vortex exists when instantaneous streamlines mapped onto a plane normal to the vortex core exhibit a roughly circular or spiral pattern when viewed from a reference moving with the center of the vortex core."

For compressible flows, as suggested by Kolář [44], the volume change due to compression and expansion should be deducted, and the traceless part $\boldsymbol{D^*}$ should be used. The definition of λ_{ci} then becomes the imaginary part of the complex eigenvalue λ_c of $\boldsymbol{D^*}$.

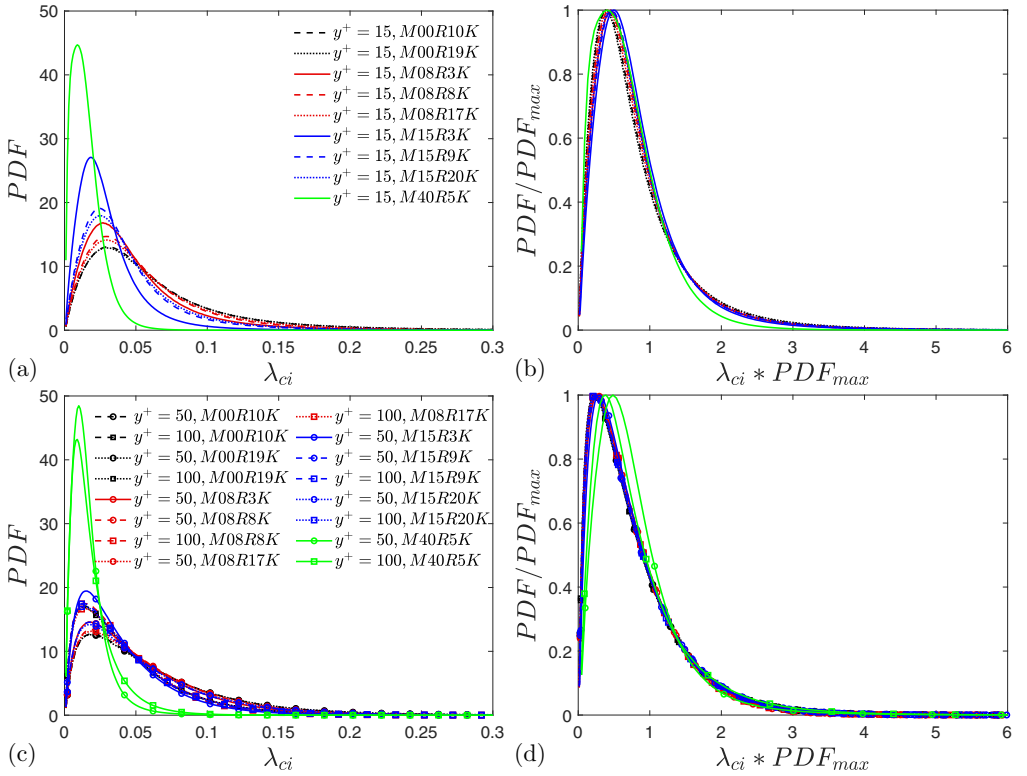

FIG. 1. PDFs of λ_{ci} in the buffer layer ($y^+ \approx 15$) are shown in (a), and those in the logarithmic region ($y^+ \approx$ 50 and 100) are shown in (c) for the compressible turbulent channel flows in Table I and the two incompressible cases; the corresponding PDFs normalized by their own maximum ($\mathrm{PDF_{max}}$) in the buffer layer are shown in (b), and those in the logarithmic region are shown in (d).

A. Swirling strength and threshold

The imaginary part λ_{ci} indicates the local swirl strength as shown by Zhou *et al.* [39] and a suitable threshold is needed to extract vortices. A new feature of the probability density function (PDF) of the swirl strength is observed by Wang *et al.* [21] and described as follows. While the PDF of swirl strength varies with the wall-normal distance and the Reynolds number, PDFs normalized by the corresponding maximum ($\mathrm{PDF_{max}}$) are able to collapse onto a single curve. Thus, the product of $\mathrm{PDF_{max}}$ and the corresponding swirling strength ($\lambda_{ci}^{\mathrm{corr}}$), which is defined as $\eta = \mathrm{PDF_{max}} \cdot \lambda_{ci}^{\mathrm{corr}}$, remains constant for all the cases. This new observation allows a uniform threshold ($\lambda_{ci,\mathrm{thre}}$) to be applied to PIV and DNS databases with different grid resolutions, which is the most probable swirl strength estimated by $\lambda_{ci,\mathrm{thre}} = \eta/\mathrm{PDF_{max}}$. Wang *et al.* [21] test a variety of thresholds, η ranging from 0.2 to 0.6, and obtain similar results. The current paper examines η within the interval [0.2,0.4], and presents its robustness in Appendix B.

The present work utilizes the same strategy as Wang *et al.* [21] to determine the threshold. The PDFs of λ_{ci} from different wall-normal distances scaled by both the wall unit and semilocal scaling are examined. In Figs. 1(a) and 1(c) and Figs. 2(a) and 2(c), the PDF curves vary with the wall-normal position, Mach number, and Reynolds number, while the normalized PDFs have a better collapse as shown in Figs. 2(b) and 2(d) and Figs. 1(b) and 1(d), which is consistent with incompressible flows as remarked by Wang *et al.* [21]. Figs. 1(b) and 1(d) show that for relatively lower Mach numbers $\mathrm{Ma}_b = 0.8$ and 1.5, the normalized PDFs in the buffer layer and the logarithmic region have a satisfactory collapse separately, but this phenomenon disappears for the

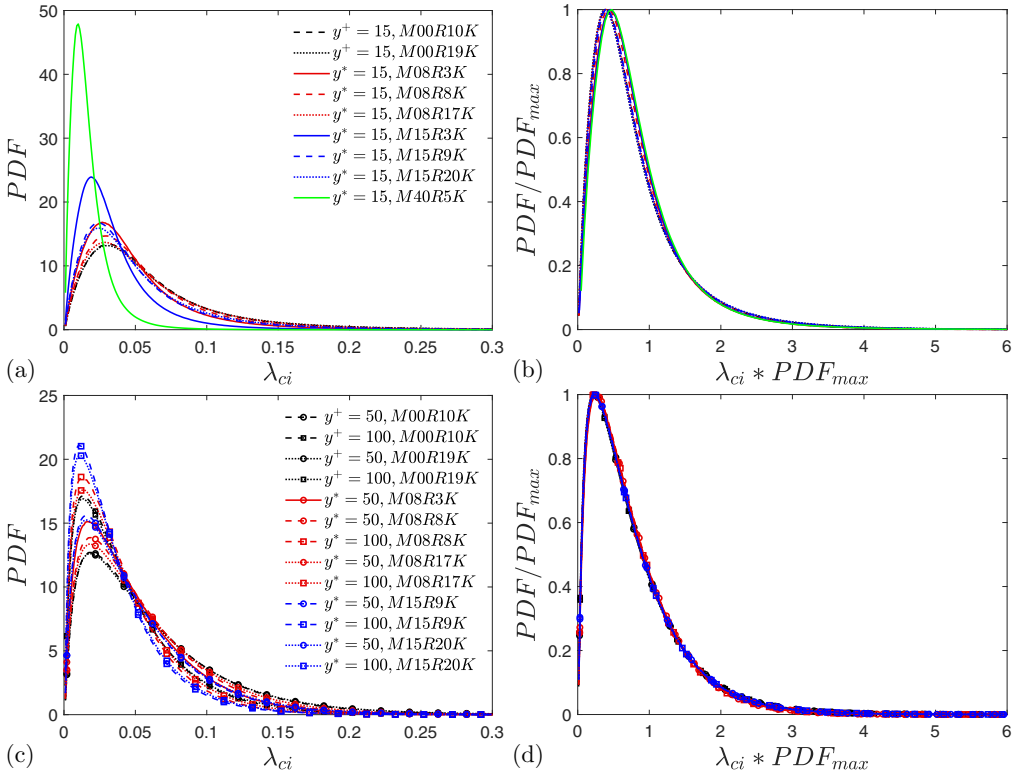

FIG. 2. PDFs of λ_{ci} in the buffer layer ($y^* \approx 15$) are shown in (a), and those in the logarithmic region ($y^* \approx 50$ and 100) are shown in (c) for the compressible turbulent channel flows in Table I and the two incompressible cases; the corresponding PDFs normalized by their own maximum ($\mathrm{PDF_{max}}$) in the buffer layer are shown in (b), and those in the logarithmic region are shown in (d).

higher Mach number case $\mathrm{Ma}_b = 4$. In the semilocal scaling [Figs. 2(b) and 2(d)], the normalized PDFs of all Mach number cases considered are able to collapse well due to the effectiveness of the semilocal scaling to account for the compressibility effect, especially for hypersonic flows. Huang *et al.* [45], Coleman *et al.* [46], and Patel *et al.* [47] also report the better performance of the semilocal scaling than the wall unit for compressible flows. Based on the argument above, the most probable λ_{ci} can still work as a uniform threshold in the semilocal scaling among different cases for compressible flows, and the product η should be different for the buffer layer ($y^* = 15$) and the logarithmic region ($y^* > 50$).

In order to determine the threshold explicitly, product η distributions with respect to the wall-normal position in the wall unit and the semilocal scaling are plotted in Fig. 3. As shown in Fig. 3(a), when the wall-normal distance is scaled by the wall unit, there is no uniform distribution among cases. In Fig. 3(b), all the distributions of η decrease sharply beginning from $y^* \approx 10$–12 and level off to 0.20–0.25 at $y^* \approx 50$. This similarity allows a uniform threshold applicable to different cases and further implies the effectiveness of the semilocal scaling in compressible flows as well. By averaging the products from all the data considered, the threshold ($\lambda_{ci,\mathrm{thre}}$) is determined to be the most probable swirl strength corresponding to $\lambda_{ci,\mathrm{thre}} = 0.39/\mathrm{PDF_{max}}$ for $y^* \approx 15$ and $\lambda_{ci,\mathrm{thre}} = 0.22/\mathrm{PDF_{max}}$ for the logarithmic region with $y^* > 50$. The robustness of this threshold has been examined by varying it from $0.20/\mathrm{PDF_{max}}$ to $0.40/\mathrm{PDF_{max}}$ and a similar most probable vortex orientation is obtained.

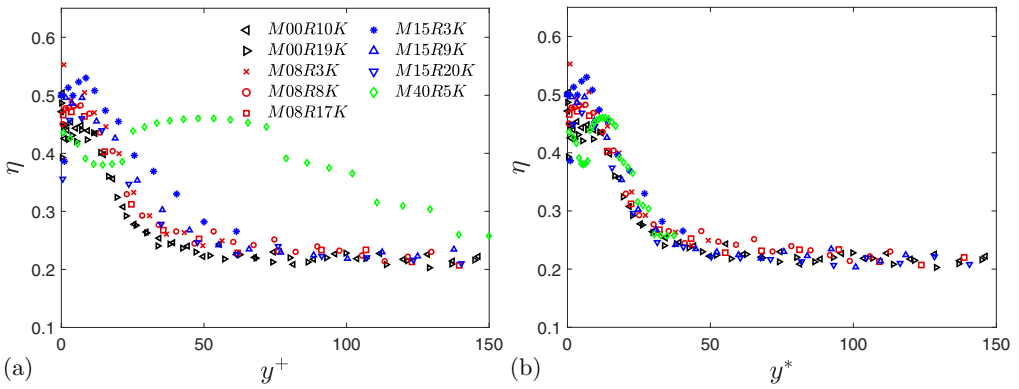

FIG. 3. (a) The distribution of the product η with respect to the wall-normal position in the wall unit for the compressible turbulent channel flows in Table I and the two incompressible cases; (b) the η distribution with respect to the wall-normal position in the semilocal scaling.

B. Vortex orientation

The present study employs the eigenvector $\boldsymbol{v}_r$ corresponding to the real eigenvalue λ_r to characterize the orientation of the vortex following the work by Zhou [48] and Zhou *et al.* [39]. The real eigenvector $\boldsymbol{v}_r$ could be in two opposite directions in space by changing its sign. The one which forms an acute angle with the vorticity $\boldsymbol{\omega}$ is considered and $\boldsymbol{v}_r$ is a unit vector that is normalized by its own norm. For a three-dimensional (3D) vector, two angles θ_{xy} and θ_{-zx} as defined in Fig. 4 would be sufficient to characterize the vortex orientation. The real eigenvector $\boldsymbol{v}_r$ is projected on the x-y plane and the x-z plane, which gives projection vectors $\boldsymbol{v}_{r,xy}$ and $\boldsymbol{v}_{r,-zx}$ separately. In the x-y plane, the angle between the x axis and the projection vector $\boldsymbol{v}_{r,xy}$ is defined as θ_{xy}. In the x-z plane, the angle between the negative z axis and the projection vector $\boldsymbol{v}_{r,-zx}$ is defined as θ_{-zx}. These definitions are consistent with Gao *et al.* [20] and Wang *et al.* [21].

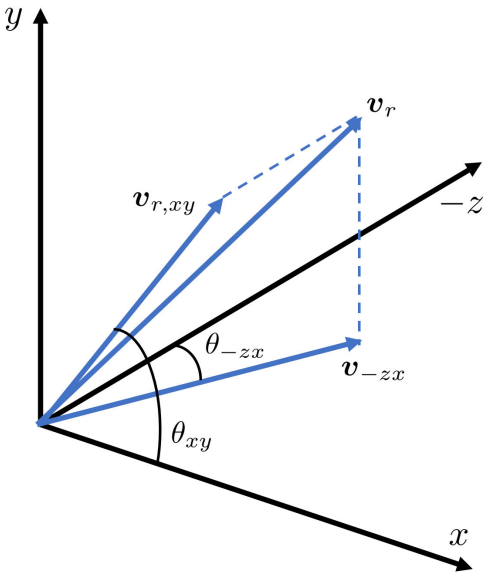

FIG. 4. Sketch for defining characteristic projection angles of the vortex orientation.

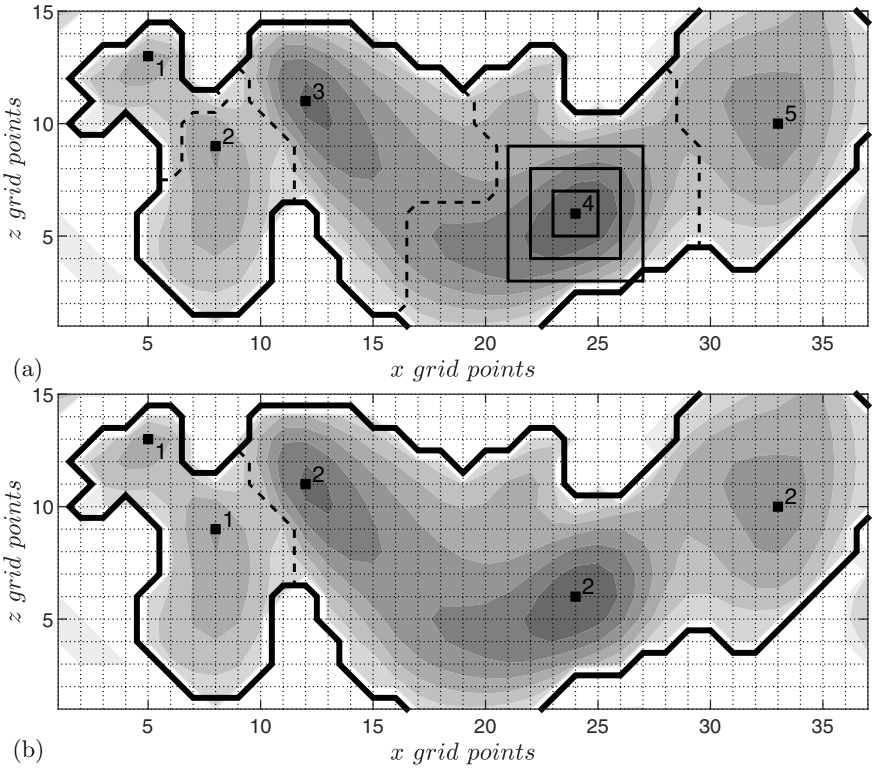

FIG. 5. Sketch for the identification and combination of vortex cores. Instantaneous contours of λ_{ci} extracted from Case M15R9K at $y^* \approx 50$ are in gray. (a) The local maximum is implied by a small square and an index. The thick solid lines surround the region exceeding the λ_{ci} threshold. The dashed line represents the boundary between cores in the saddle region. Squares in the solid line around Peak 4 are shown to clarify the vortex identification algorithm; (b) the identified vortex cores after the combination step are shown. The local maximum is implied by a small square as well, and their indices denote the core number they belong to.

C. Identification technique for vortices

Besides the vortex orientation, the vortex size and strength are also of great significance. To evaluate them, an individual vortex which is defined as a connected region consisting of grid points with their swirling strength beyond the threshold has to be identified. Afterward, these vortices are called vortex cores or cores. Gao *et al.* [20] develop a region-growing algorithm based on the one from Ganapathisubramani *et al.* [49] to identify vortex cores. In this work, the identification algorithm is improved from the one in Gao *et al.* [20] and consists of a series of steps described as follows.

Step 1: All points whose swirl strength exceeds the threshold stand a chance of forming vortex cores. In Fig. 5, the region enclosed by the solid line represents grid points with swirl strength beyond the threshold mentioned in Sec. III A.

Step 2: Each point has eight neighbors. All the peaks whose swirl strength is larger than all their neighbors are marked by a small square and indexed in order, as shown in Fig. 5(a).

Step 3: In order to determine the extent of vortex cores, a series of squares of different sizes is set to surround a peak, e.g., Peak 4, as shown in Fig. 5(a). For each peak, this series of squares is scanned from the innermost one to the outer one in sequence. A free point, which is not assigned to any vortex cores, on the side of squares scanned is assigned to this core if the following two conditions are satisfied: (i) Its swirl strength is smaller than that of the nearest one on its nearby

inner scanned square and (ii) the corresponding neighbor point has been considered as belonging to this core. Referring to vertex points, the conditions become the following: (i) its swirl strength is smaller than that of any neighbors on either the same or its nearby inner scanned square and (ii) the same as side points. The scanning procedure stops when there is no point detected on a single square. This step provides a rough estimation of the extent and one more step is required to give the precise edge.

Step 4: The sequential scanning from the innermost square to those outer ones described in Step 3 is repeated in this step, but different criteria are applied. A point on both sides and vertexes is assigned if its swirl strength is smaller than that of any neighbors on the same or the nearby inner scanned square, and the corresponding neighbor point has been considered to belong to this core. To eliminate its dependence on the scanning direction, a square is scanned first counterclockwise and later clockwise.

Step 5: A combination algorithm is implemented. Some vortex cores may connect to each other and stand a chance to merge, such as Cores 1–5 in Fig. 5. The local vortex orientation is characterized by the real eigenvector $\boldsymbol{v}_r$. If the angle difference between any pair of neighboring points crossing the edge of two connected cores is smaller than a threshold α_c, then these two cores are merged into a single one. The current strategy follows the threshold by Gao *et al.* [20], where $\alpha_c = 10^\circ$. Taking Cores 1–5 shown in Fig. 5(a) for example, Cores 1 and 2 merge into one core, and Cores 3–5 merge into another one in Fig. 5(b).

Step 6: According to Gao *et al.* [20], in-plane cores with elevation angle α_e less than 10° are eliminated after the identification of vortex cores, where α_e is the angle formed by the averaged real eigenvector $\overline{\boldsymbol{v}_r}$ and the x-z plane. Weaker vortex cores whose radii in the semilocal scaling are smaller than 8 are also eliminated, as suggested by Gao *et al.* [20]. Additionally, the vortex cores truncated by sides of the statistical region applying the above steps (not necessarily the computational domain) are ignored as well.

D. Vortex core radius and circulation

Now that, with the vortex cores extracted, the vortex size and strength can be quantified by the radius and circulation of vortex cores, respectively. In incompressible flows, Gao *et al.* [20] estimate the local circulation by the component of vorticity parallel to the vector $\boldsymbol{v}_r$. The vortex core circulation is the integration of the local one over one core's in-plane area

$$\Gamma^+ = \iint_{A^+} (\boldsymbol{\omega}^+ \cdot \boldsymbol{v}_r)(\boldsymbol{v}_r \cdot \boldsymbol{n}_y)\, dx^+ dz^+, \tag{1}$$

where A^+ is the in-plane area evaluated by multiplying the number of grid points of an individual vortex core with the cell area ($\triangle x^+ \cdot \triangle z^+$), $\boldsymbol{\omega}^+$ indicates the vorticity in the wall unit, $\boldsymbol{n}_y$ is the unit normal vector of the x-z plane, and $\overline{\boldsymbol{v}_r}$ is the averaged unit real eigenvector throughout an individual vortex core.

The vortex core radius is computed as

$$r^+ = \sqrt{\overline{\boldsymbol{v}_r} \cdot \boldsymbol{n}_y \cdot A^+}. \tag{2}$$

Here the radius of a vortex is not calculated directly from the in-plane area but from its projection area onto the plane orthogonal to the vector $\overline{\boldsymbol{v}_r}$.

To estimate the minimum radius, Gao *et al.* [20] consider the vortex cores composed of at least two grid points and the corresponding minimum radius is evaluated by Eq. (2) using the grid spacing (12.4 wall units) and the most probable inclination angle 45° in the logarithmic region. Regarding the compressible cases concerned in this work, the semilocal scaled circulation Γ^* and radius r^* are defined as $\Gamma^+(\rho/\rho_w)/(\mu/\mu_w)$ and $r^+\sqrt{\rho/\rho_w}/(\mu/\mu_w)$, respectively, and the minimum radius threshold of 8.0 is applied to the variable r^*.

IV. RESULTS AND DISCUSSIONS

In this section, statistical features including the inclination angle, convection velocity, radius, circulation, and population of vortices are investigated. Instantaneous structures and streaks together with their connections are shown and explained in Sec. IV A. The left subsections can be divided into two main parts according to their statistical strategy. Instead of applying the improved region-growing algorithm, a much simpler statistical method is employed in Secs. IV B and IV C, i.e., all grid points with the swirling strength exceeding the threshold are taken into account. The reason is that the vortex core identification algorithm only considers vortices crossing the x-z plane and ignore the in-plane vortices as claimed by Wang *et al.* [21]. Since both the in-plane and cross-plane vortices exist in the real flow field, this simpler method could provide more realistic results. On the other hand, the improved region-growing algorithm described in Sec. III C is necessary to estimate the size, strength, and population of vortices in Secs. IV D and IV E. Finally, a quantitative model of vortices based on a set of ODEs can be found in Sec. IV G.

A. Instantaneous vortex structures

The instantaneous vortex and velocity fluctuation field from Case M15R9K are examined in Fig. 6. The 3D view of vortex structures [see Fig. 6(a)] is extracted by the isosurface of the swirling strength $|\lambda_{ci}| \approx 0.06$ (approximately 10% of its maximum in the visualized region), and the color from yellow to red indicates their wall-normal distance from $y^* \approx 15$ to $y/h \approx 0.4$. It is observed that most vortices lean downstream. Vortex arches, quasistreamwise vortices, and symmetric and asymmetric hairpin vortices can be found in Fig. 6(a). Figure 6(b) shows the alternating pattern of elongated high-speed and low-speed streaks with a length of $O(1000)$ wall units in the logarithmic region using the streamwise velocity fluctuation u'^+. Figure 6(c) shows the same fluctuation field with Fig. 6(b), where vortex structures extracted using the method of Fig. 6(a) are also displayed. Through the comparison of Figs. 6(b) and 6(c), most vortices populate around low-speed streaks since low-speed streaks are recognized to be induced by the moving hairpin leg [50]. This close connection is also reported by Jiménez and Pinelli [51] and Ringuette *et al.* [52] in incompressible flows, and Pirozzoli *et al.* [19] in a compressible turbulent boundary layer at $\mathrm{Ma} = 2$.

One can also see more instantaneous structures of interest in Fig. 7. Figure 7(a) highlights a vortex that has a similar shape to the theoretical Ω-shaped model in Sec. IV G by the green dotted line. There is one more Ω-shaped vortex in Fig. 6(a) centering at location (800,200). This consistency illustrates that the theoretical Ω-shaped model proposed in Sec. IV G could potentially serve as an appropriate estimation of the topology of vortex structures. Figure 7(b) exhibits a hairpin vortex packet near the wall, which encompasses around three vortices. These vortices align coherently in the streamwise direction and distribute with a distance of $O(100)$ wall units to form longer structures. The vortex packet is a typical feature well investigated in incompressible wall turbulence [21,53]. Our finding here further verifies its existence in compressible channel flows at moderate Reynolds and Mach numbers.

Figure 8 presents instantaneous vortex cores identified by the technique described in Sec. III C and the corresponding λ_{ci} field from Case M15R9K at $y^* \approx 100$. At all three specific wall-normal distances, the identified connected region has a similar shape, with the contour of λ_{ci} representing positions with λ_{ci} exceeding the corresponding threshold. The number of grid points with a swirling strength larger than the threshold but not assigned to any vortex cores after applying the present method is less than 0.1%. The other two wall-normal locations $y^* \approx 15$ and 50 are also examined, although not shown here, and similar results can be obtained. Therefore, the current identification technique is able to capture most vortex structures effectively.

B. Vortex orientation

To study the vortex orientation, its distributions and variations are illustrated. According to the ideal hairpin vortex model, the statistic of the vortex orientation could be symmetric, and these

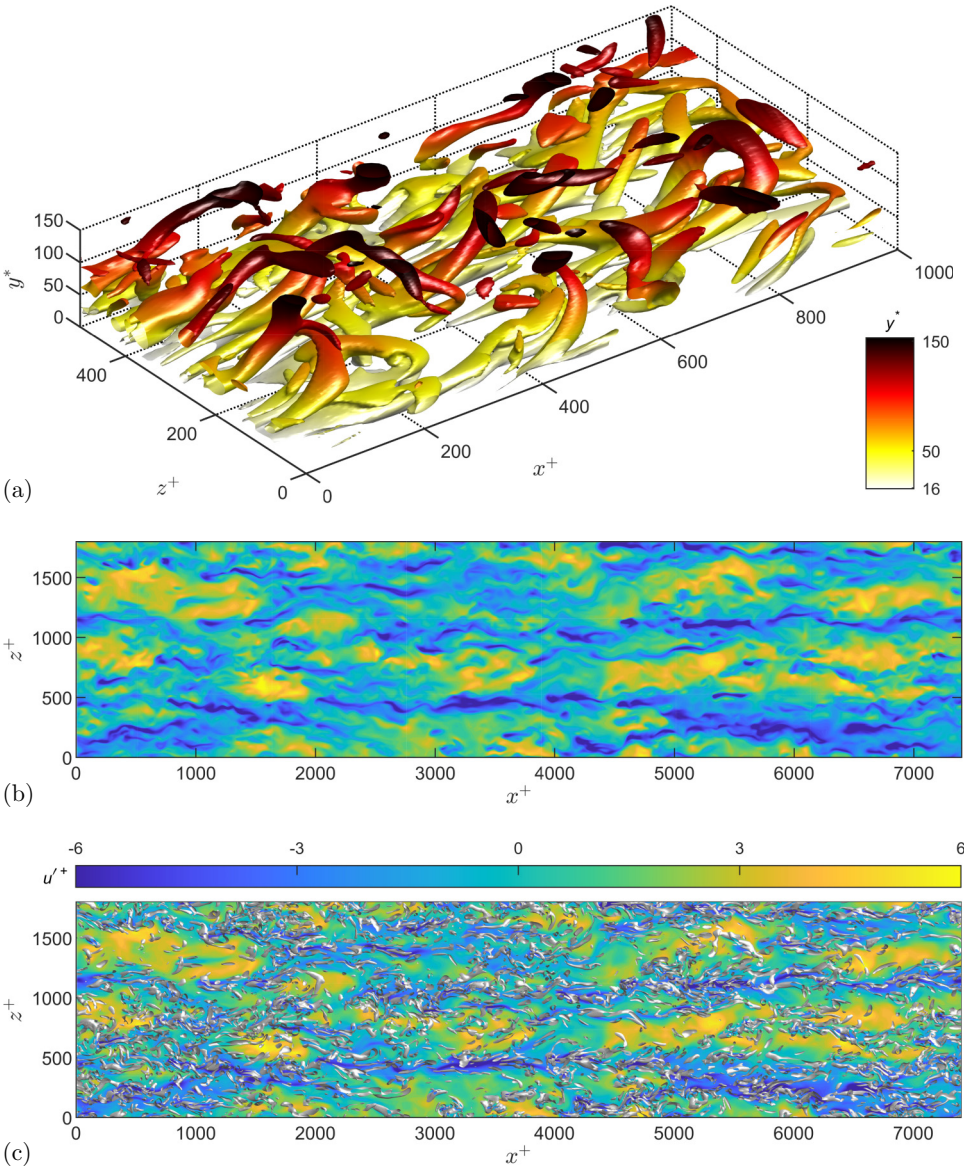

FIG. 6. (a) Visualization of instantaneous vortex structures from Case M15R9K using the λ_{ci} criterion with a threshold $|\lambda_{ci}| \approx 0.06$ (the color indicates the wall-normal distance from $y^* \approx 15$ to $y/h \approx 0.4$); (b) contours of the streamwise velocity fluctuation u'^+ at $y^* \approx 50$ from Case M15R9K; (c) contours of u'^+ and extracted vortex structures identified by the λ_{ci} criterion with a threshold $|\lambda_{ci}| \approx 0.06$ at $y^* \approx 50$ from Case M15R9K.

patterns can be observed in PDF curves of inclination angle θ_{xy} and θ_{-zx} using DNS of channel flows in Table I and the incompressible reference in Figs. 9 and 10. There is an axisymmetric property with respect to 0° for the PDF of θ_{-zx}, i.e., $P(\theta_{-zx}) \approx P(-\theta_{-zx})$, while regarding the PDF of θ_{xy}, it becomes a periodic function with a period of 180°, i.e., $P(\theta_{xy}) \approx P(\theta_{xy} \pm 180°)$. To simplify the description, only the angle within 0°–180° will be reported in the following discussion.

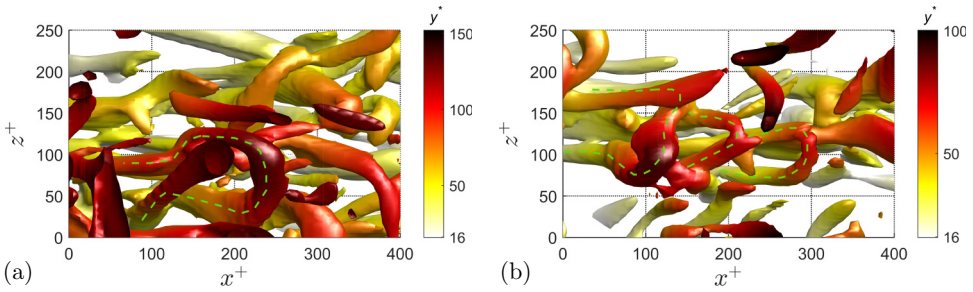

FIG. 7. Some representative instantaneous structures from Case M15R20K using the λ_{ci} criterion with a threshold $|\lambda_{ci}| \approx 0.06$ (the color indicates the wall-normal distance from $y^* \approx 15$ to 150): (a) A vortex shares a similar shape to the theoretical model in Sec. IV G; (b) a streamwise-aligned vortex packet in the near-wall region.

1. Probability density for the vortex orientation angle

PDFs are computed with instantaneous data to characterize the relative frequency of instantaneous vortex orientation angles. Figure 9 plots PDF curves of inclination angle θ_{xy} and θ_{-zx} in the buffer layer ($y^+ \approx 15$) and the logarithmic region ($y^+ \approx 50$ and 100). At $y^+ \approx 15$ [see Figs. 9(a) and 9(d)], the peak of PDF curves is around 1°–6° for θ_{xy}, and 78°–82° for θ_{-zx}, indicating a relative agreement of the most probable angle across all cases. However, in the logarithmic region, there is a wider range of the most probable angle of each case, e.g., 6°–28° for θ_{xy} and 64°–82° for θ_{-zx} at $y^+ \approx 100$ [Figs. 9(c) and 9(f)]. It is worth mentioning that PDF curves of Case M40R5K have an even different shape compared with those of lower Ma_b and incompressible cases.

Figure 10 contains similar curves as Fig. 9 but nondimensionalized with the semilocal scaling. In the buffer layer, the most probable angle is 4°–7° for θ_{xy} [Fig. 10(a)] and 80°–83° for θ_{-zx} [Fig. 10(d)]. In the logarithmic region, at $y^* \approx 50$ [Figs. 10(b) and 10(e)], the peak occurs between $17° < \theta_{xy} < 19°$ and $80° < \theta_{-zx} < 82°$; at $y^* \approx 100$ [Figs. 10(c) and 10(f)] the peak occurs between $31° < \theta_{xy} < 33°$ and $63° < \theta_{-zx} < 65°$. At the position far away from the wall, the PDFs of θ_{-zx} [see Fig. 10(f)] plateau around its peak to 0°, and the corresponding probability density varies by less than 20%. Overall, Fig. 10 shows a better consistency of not only the most probable angles

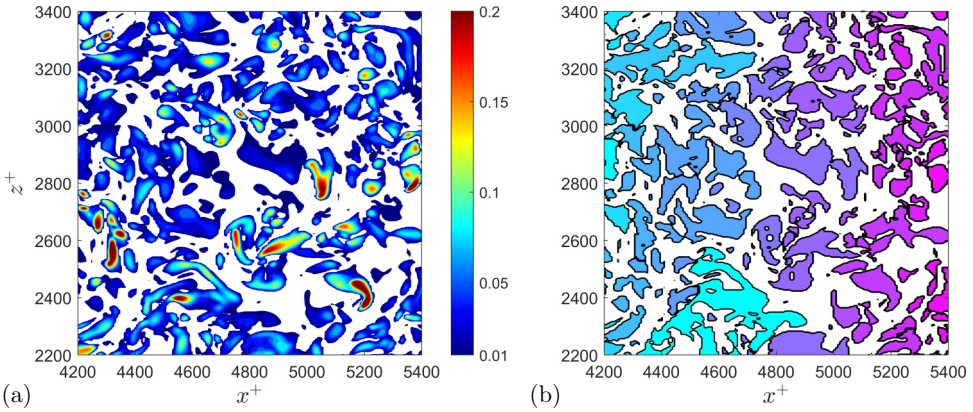

FIG. 8. (a) The instantaneous field of λ_{ci} from Case M15R9K at $y^* \approx 15$, where regions with a swirling strength exceeding the corresponding threshold are colored; (b) the vortex cores in the same region with (a) after applying the identification technique described in Sec. III C, where an individual vortex core is a colored region bounded by the black line, and different colors denote different cores.

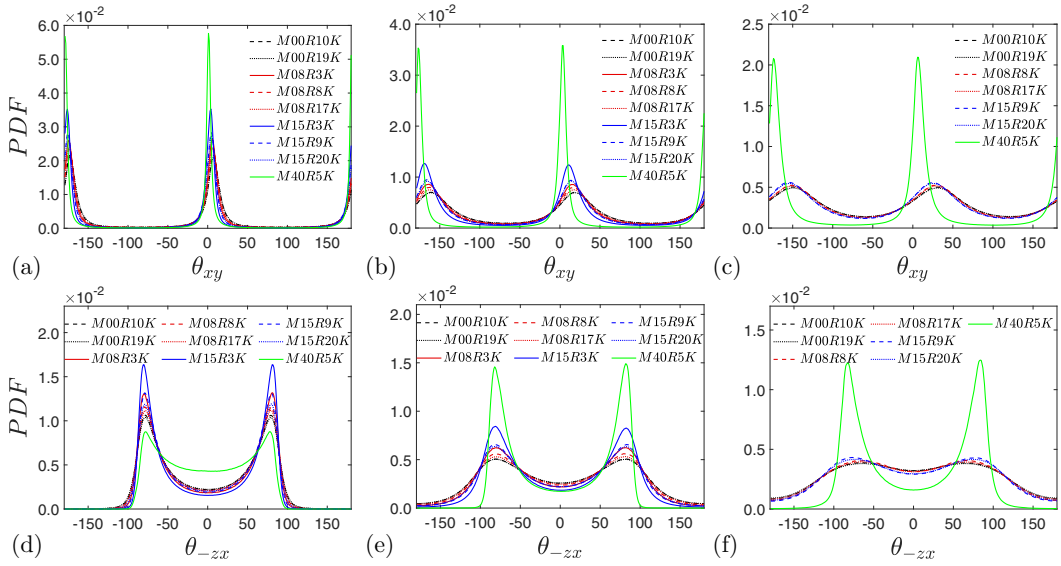

FIG. 9. PDFs of θ_{xy} and θ_{-zx} based on $\boldsymbol{v}_r$ using the DNS database in Table I and the two incompressible cases. The PDFs of θ_{xy} are plotted in the first row; θ_{-zx} in the second row. The first column presents the statistics at $y^+ \approx 15$, the second one at $y^+ \approx 50$, and the third one at $y^+ \approx 100$. Cases are denoted using the consistent color and line style as defined in Sec. II.

but their general shape as well, especially in the logarithmic region. Through this comprehensive comparison, it is reasonable to draw the following conclusion: (i) the inconsistency of the most probable angle and the shape of the PDF curve is due to the nondimensionalization by wall units instead of semilocal units. The latter is able to provide a satisfactory collapse of the PDF curves in the logarithmic region. The success of semilocal scaling further validates Morkovin's hypothesis [26] in vortical structures; (ii) the influence of Re_τ^* (145–934) and Ma_b (0, 0.8 and 1.5) on the distribution of the vortex orientation is limited if the semilocal scaling is used.

*2. Orientation variation with the wall-normal distance y**

The previous subsection presented PDFs of orientation angles at select wall-normal distances. In order to further investigate the wall-normal variation of the vortex orientation, contours of corresponding PDFs from $y^* \approx 15$ to 150 utilizing the DNS database in Table I and two incompressible cases are shown in Fig. 11 for θ_{xy} and in Fig. 12 for θ_{-zx}. Results from cases with the same Ma_b are shown in one row, and for each row, cases are arranged in order of Re_τ^*. The most probable θ_{xy} and θ_{-zx} are highlighted by the dotted line (.....), and their corresponding vertical asymptotic lines are denoted by dashed lines (_ _ _ _ _).

Foremost, in Figs. 11 and 12, all the considered cases from different Re_τ^* and Ma_b including the incompressible cases share a similar variation tendency after applying the semilocal scaling as discussed in Sec. IV B 1. With the increase of y^*, the most probable θ_{xy} increases monotonically throughout both the buffer layer and the logarithmic region. At $y^* \approx 150$ and higher wall-normal positions (not shown), the most probable θ_{xy} approaches 45° as reported by a number of studies [1,54,55]. The increasing feature of θ_{xy} up to 45° in the logarithmic region could statistically correspond to the right leg of the ideal hairpin vortex model, which is recognized to lean downstream at an angle of 45°, and the other most probable θ_{xy} approaching −135° could correspond to the left leg. As regards θ_{-zx}, in the buffer layer, the most probable θ_{-zx} remains almost constant at about 80° indicating the dominant existence of quasistreamwise vortices [9]. In the logarithmic region, the high probability at $\theta_{-zx} \approx 0°$ implies the hairpin neck (inward) and head. The variation tendency of

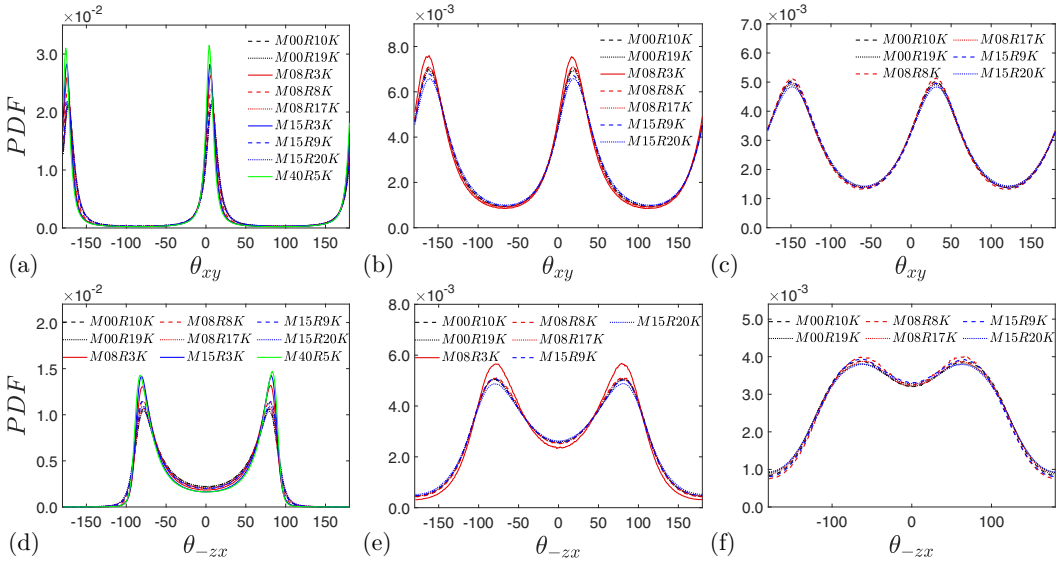

FIG. 10. PDFs of θ_{xy} and θ_{-zx} based on $\boldsymbol{v}_r$ using the DNS database in Table I and the two incompressible cases. The PDFs of θ_{xy} are plotted in the first row and θ_{-zx} in the second row. The first column presents the statistics at $y^* \approx 15$, the second one at $y^* \approx 50$, and the third one at $y^* \approx 100$. Cases are denoted using the consistent color and line style as defined in Sec. II.

θ_{xy} and θ_{-zx} is consistent with the report of Wang *et al.* [21] in incompressible flows. Moreover, the findings that the quasistreamwise vortices dominate in the buffer layer, and archlike vortices become more common in the logarithmic region, agree well with the DNS investigation of Robinson [9] in incompressible flows.

3. Compressibility effects on the vortex orientation

In previous sections, it is concluded that vortices in compressible and incompressible flows share the same orientation distribution, and θ_{xy} attains 45° as y^* increases. In this section, we discuss the impact of compressibility on vortex orientation through theoretical analysis to interpret these findings. We will begin with the evolution of the vorticity vector and then show its intrinsic connection with the real eigenvector $\boldsymbol{v}_r$.

We consider the most general form of the vorticity evolution equation [17], i.e.,

$$\frac{D\boldsymbol{\omega}}{Dt} = -\boldsymbol{\omega}(\boldsymbol{\nabla}\cdot\boldsymbol{u}) + (\boldsymbol{\omega}\cdot\boldsymbol{\nabla})\boldsymbol{u} + \frac{1}{\rho^2}\boldsymbol{\nabla}\rho\times\boldsymbol{\nabla}p - \frac{1}{\rho^2}\boldsymbol{\nabla}\rho\times(\boldsymbol{\nabla}\cdot\boldsymbol{T}) + \frac{1}{\rho}\boldsymbol{\nabla}\times(\boldsymbol{\nabla}\cdot\boldsymbol{T}), \tag{3}$$

where p is pressure, $\boldsymbol{T}$ is the stress tensor, and D/Dt is the substantial derivative. For incompressible flows, this equation can be simplified into $D\boldsymbol{\omega}/Dt = (\boldsymbol{\omega}\cdot\boldsymbol{\nabla})\boldsymbol{u} + \nu\nabla^2\boldsymbol{\omega}$, where ν is the kinematic viscosity. The first term of the right-hand side represents vortex stretching which produces vorticity, and the second term is viscous diffusion of vorticity. Noting that $\boldsymbol{\nabla u} = \boldsymbol{S} + \boldsymbol{\Omega}$ and $\boldsymbol{\Omega}\cdot\boldsymbol{\omega} = 0$, the stretching term can be rewritten as $(\boldsymbol{\omega}\cdot\boldsymbol{\nabla})\boldsymbol{u} = (\boldsymbol{\nabla u})\cdot\boldsymbol{\omega} = \boldsymbol{S}\cdot\boldsymbol{\omega}$, where $\boldsymbol{S}$ is the rate-of-strain tensor and $\boldsymbol{\Omega}$ is the rotation tensor. Since vortex stretching is the dominant production term, root-mean-square vorticity will follow the maximum stretching direction of the material line element [21,55], i.e., the principal axis of the $\boldsymbol{S}$. In a statistical sense, one can expect turbulent channel flows to

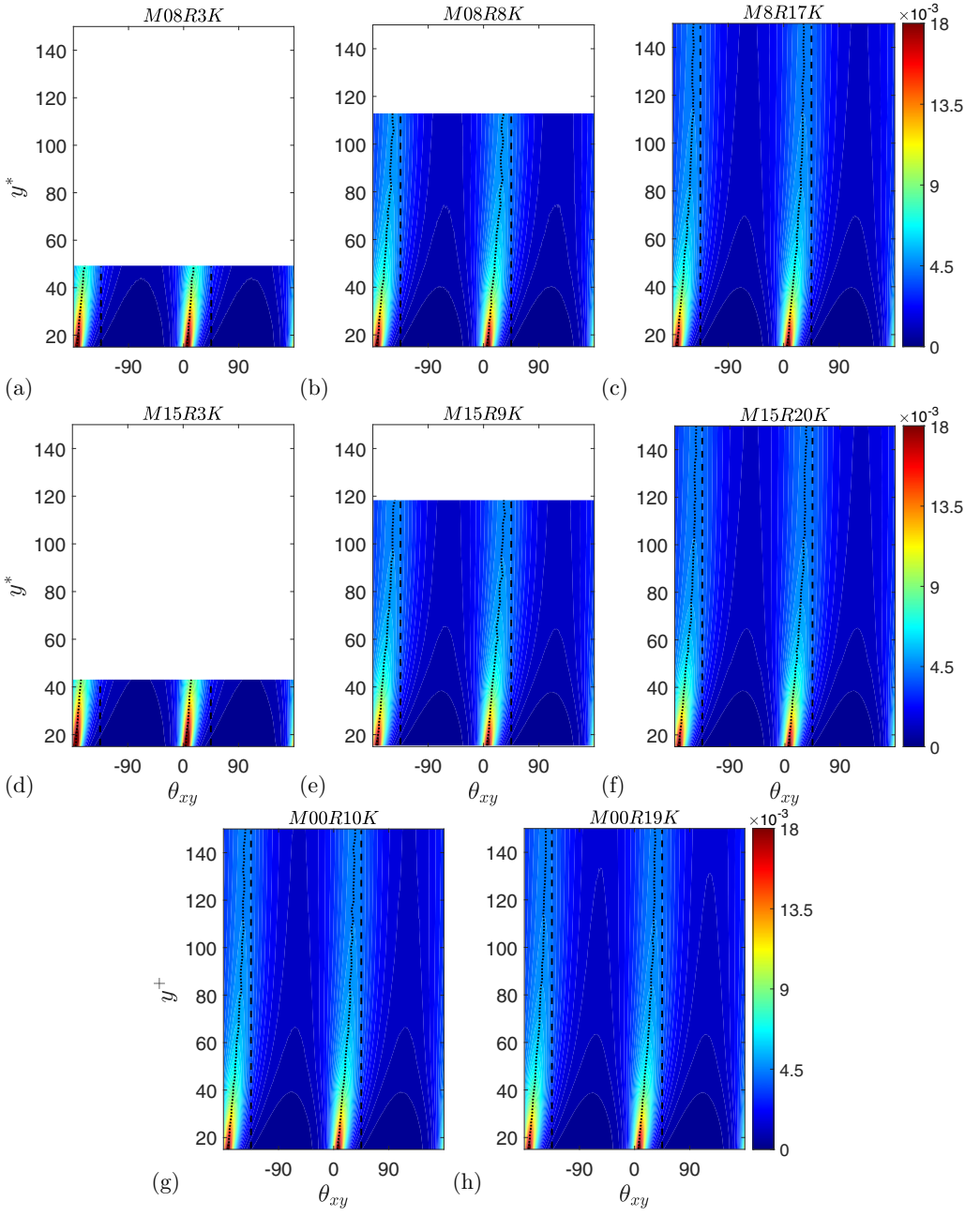

FIG. 11. Contours for the PDFs of θ_{xy} based on $\boldsymbol{v}_r$ varying with respect to y^* in the range of 15 to 150 using the DNS database in Table I and the two incompressible cases. The first row presents the statistics from cases with $\mathrm{Ma}_b = 0.8$: (a) Case M08R3K, (b) Case M08R8K, and (c) Case M08R17K; the second row $\mathrm{Ma}_b = 1.5$: (d) Case M15R3K, (e) Case M15R9K, and (f) Case M15R20K; the third row from incompressible cases: (g) Case M00R10K and (h) Case M00R19K. The dashed lines (- - - - -) denote $\theta_{xy} = 45^\circ$ or -135°; the dotted lines (.....) denote the most probable θ_{xy} at different wall-normal positions. All figures share the same color bar.

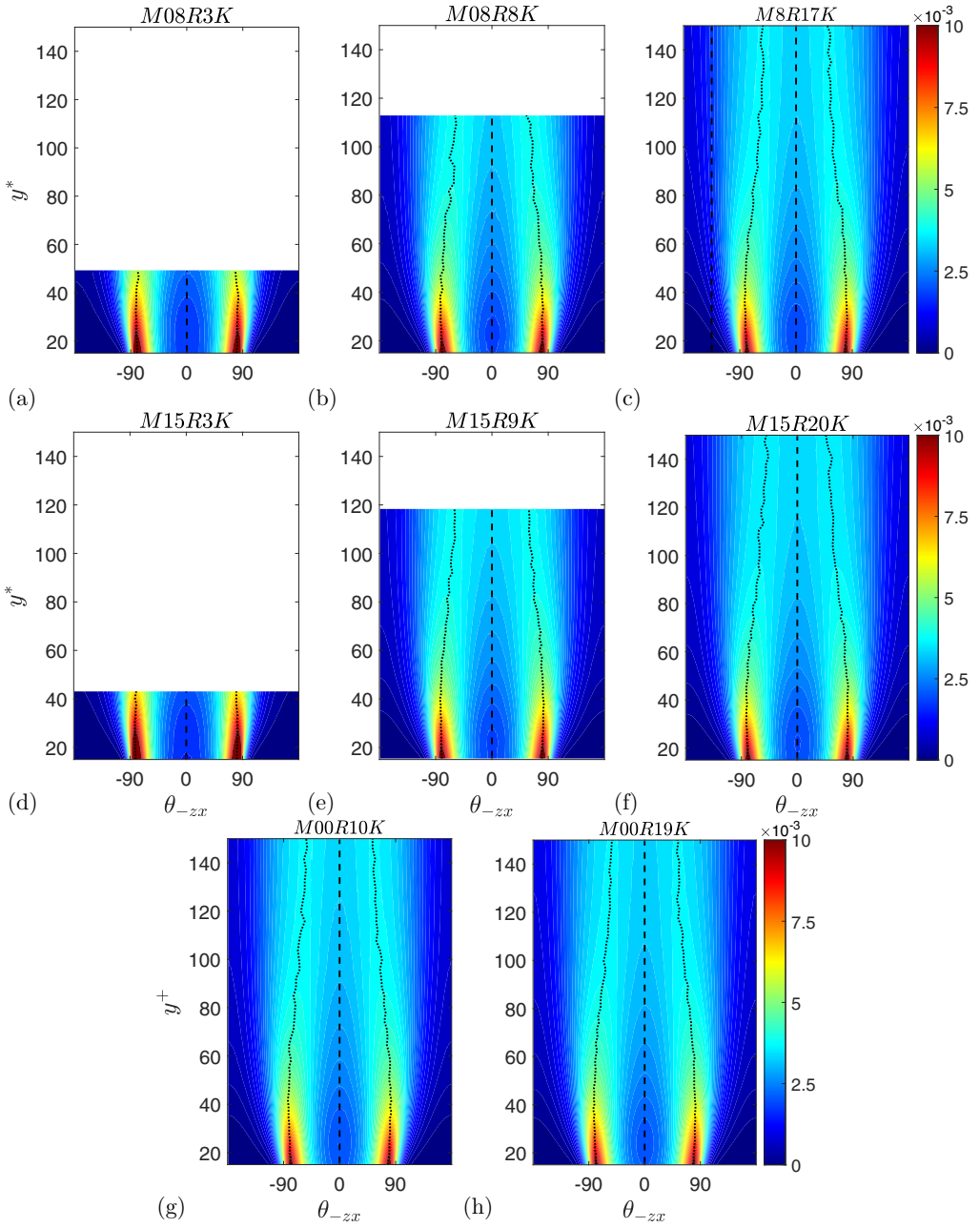

FIG. 12. Contours for the PDFs of θ_{-zx} based on $\boldsymbol{v}_r$ varying with respect to y^* in the range of 15 to 150 using the DNS database in Table I and the two incompressible cases. The first row presents the statistics from cases with $\mathrm{Ma}_b = 0.8$: (a) Case M08R3K, (b) Case M08R8K, and (c) Case M08R17K; the second row $\mathrm{Ma}_b = 1.5$: (d) Case M15R3K, (e) Case M15R9K, and (f) Case M15R20K; the third row from incompressible cases: (g) Case M00R10K and (h) Case M00R19K. The dashed lines (- - - - -) denote $\theta_{-zx} = 0^\circ$; the dotted lines (.....) denote the most probable θ_{xy} at different wall-normal positions. All figures share the same color bar.

regress to two-dimensional (2D) shear flows with the mean rate-of-strain tensor $\overline{\boldsymbol{S}}$,

$$\overline{\boldsymbol{S}} = \begin{bmatrix} \frac{\partial \overline{u}}{\partial x} & \frac{1}{2}\frac{\partial \overline{u}}{\partial y} \\ \frac{1}{2}\frac{\partial \overline{u}}{\partial y} & \frac{\partial \overline{v}}{\partial y} \end{bmatrix}, \tag{4}$$

and the corresponding principal axis is

$$\theta = \frac{1}{2}\arctan\left(\frac{\partial \overline{u}/\partial y}{\partial \overline{u}/\partial x - \partial \overline{v}/\partial y}\right). \tag{5}$$

It is conspicuous from Eq. (5) that $\theta = 45^\circ$ for channel flows; $\theta = 45^\circ$ corresponds to the condition $\overline{\omega_x^2} = \overline{\omega_y^2}$. Such a rather isotropic result can be expected for regions away from the wall [55].

Regarding compressible channel flows, the first term on the right-hand side of Eq. (3) reveals the compressibility effect. Clarifying its influence requires a more straightforward configuration. Let us consider an element of a vortex tube with a uniform density in an inviscid and barotropic flow and assume that the element is compressed in the direction perpendicular to the local vorticity vector (no vortex stretching); Eq. (3) can be simplified into $D\boldsymbol{\omega}/Dt = -\boldsymbol{\omega}(\boldsymbol{\nabla}\cdot\boldsymbol{u})$ or in tensor notation $D\omega_i/Dt = -\omega_i \partial u_j/\partial x_j$. The compression of fluid elements ($\boldsymbol{\nabla}\cdot\boldsymbol{u} < 0$) strengthens the local vorticity. However, it does not alter the vorticity direction because $\boldsymbol{\nabla}\cdot\boldsymbol{u}$ works as a uniform factor for all the vorticity components, and vorticity is intensified. The mean dilatation in this term is much smaller than the main strain for the present data up to Ma = 1.5 (see Fig. 10 in Ref. [56]), and its intensification of vorticity is negligible compared with the vortex stretching term, especially for locations away from the wall. Other terms like the third (baroclinic torque) and fourth (torque due to shear stress variation in a density-varying field) terms have no preferred direction in 2D shear flows due to the cross product of 2D vectors being perpendicular to the 2D plane. It is reasonable to conclude that the vorticity direction is still governed by the mean strain. The expression for its principal axis in Eq. (5) still holds, and the vorticity direction also attains $\theta = 45^\circ$ away from the wall in compressible channel flows.

Now that the direction of the vorticity vector has been determined, the following discussions will show its inherent connection with the real eigenvector $\boldsymbol{v}_r$ [21]. One can manipulate the vortex stretching term into

$$(\boldsymbol{\nabla u})\cdot\boldsymbol{\omega} = \boldsymbol{D}\cdot\boldsymbol{\omega} = \left(\boldsymbol{D^*} + \tfrac{1}{3}\boldsymbol{\nabla}\cdot\boldsymbol{u}\boldsymbol{I}\right)\cdot\boldsymbol{\omega} = \boldsymbol{D^*}\cdot\boldsymbol{\omega} + \left(\tfrac{1}{3}\boldsymbol{\nabla}\cdot\boldsymbol{u}\boldsymbol{I}\right)\cdot\boldsymbol{\omega}, \tag{6}$$

where $\boldsymbol{D}$ is $\boldsymbol{\nabla u}$ and $\boldsymbol{D^*}$ is the traceless part of $\boldsymbol{D}$ as defined in Sec. III. Noting that the term $(\frac{1}{3}\boldsymbol{\nabla}\cdot\boldsymbol{u}\boldsymbol{I})\cdot\boldsymbol{\omega}$ does not influence the vorticity direction for the same reason as the compressibility effect, when $\boldsymbol{\omega}$ and $\boldsymbol{v}_r$ are collinear, then $\boldsymbol{D^*}\cdot\boldsymbol{\omega} = \lambda_r\boldsymbol{\omega}$. It means if $\boldsymbol{\omega}$ aligns with $\boldsymbol{v}_r$, then it keeps its direction in the following short time interval. If not, then its direction changes towards the stretching direction indicated by the real eigenvector $\boldsymbol{v}_r$ for the reason that the vorticity component collinear with the stretching direction is intensified. At the same time, vortices are lifting away from the wall. Such an elevation converts the substantial derivative (time derivative) to a variation in the wall-normal direction [21]. It is worth mentioning that using either $\boldsymbol{D}$ or $\boldsymbol{D^*}$ leads to the same conclusion. As this work applies $\boldsymbol{v}_r$ of $\boldsymbol{D^*}$ to characterize the vortex orientation, $\boldsymbol{D^*}$ is analyzed here.

Combining the direction of vorticity and its connection with $\boldsymbol{v}_r$, the direction of $\boldsymbol{v}_r$ can be illustrated. The wall-normal change of $\theta_{xy,m}$ (the most probable θ_{xy}) for $\boldsymbol{v}_r$ and $\boldsymbol{\omega}$ is apparent in Fig. 13. In near-wall locations, the great difference between $\theta_{xy,m}$ obtained from $\boldsymbol{\omega}$ and $\boldsymbol{v}_r$ causes the critical reduction and rising of those for $\boldsymbol{\omega}$. As y^* grows beyond 150, $\theta_{xy,m}$ of $\boldsymbol{\omega}$ approaches 45° as the theoretical estimation from the mean strain (this trend is more obvious for higher Reynolds numbers). When the vorticity vector maintains its orientation, it aligns with the real eigenvector $\boldsymbol{v}_r$ based on their intrinsic relationship. We can conclude that $\boldsymbol{v}_r$ will also attain 45°, the same tendency as noticed in Sec. IV B 2, which is still valid for higher Mach numbers.

The other remark, the orientation similarity, can also be deduced from the theoretical analysis above. Similarly to the compressibility effect term, the baroclinic torque term could also be

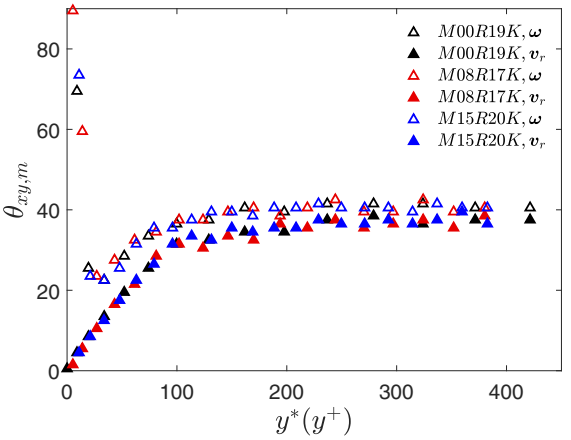

FIG. 13. The variation of the most probable θ_{xy} defined as $\theta_{xy,m}$ for the real eigenvector $\boldsymbol{v}_r$ and vorticity $\boldsymbol{\omega}$ in the wall-normal direction (semilocal scaled) using cases M00R19K, M08R17K, and M15R20K. Those for the real eigenvector $\boldsymbol{v}_r$ are denoted by filled scatters.

negligible since the pressure gradient is zero in a statistical sense. If we neglect the fourth term on the right-hand side of Eq. (3), then the vorticity evolution is governed by the vortex stretching and viscous diffusion terms, similar to the incompressible flows [57]. The postulation that the third and fourth terms of Eq. (3) have a slight effect makes sense, at least for the Mach-number range in this work for the following reason: They mainly affect the spanwise component of the vorticity vector because of the property of cross product in 2D plane discussed above, but there is no apparent difference in θ_{-zx} of the vorticity vector (not shown). Scaling the wall-normal distance in the semilocal units leads to a much better collapse of mean streamwise velocity profiles to the law of the wall [28,29] and the mean strain subsequently. Therefore, it is reasonable that the vortex orientation dominated by vortex stretching remains similar. Considering the inherent connection between the vorticity vector and eigenvector, the direction of eigenvectors is very likely to share this performance.

C. Convection velocity of vortices

Another important aspect of vortices is the convection velocity. The convection velocity denoted by U_c^+ is computed using the streamwise velocity component at the grid points recognized as vortices. The PDF of cases in Table I and the considered incompressible cases are included in Fig. 14, where U_c^+ is rescaled by the local Reynolds-averaged mean streamwise velocity U_m^+. The distribution of U_c^+/U_m^+ at $y^* \approx 15$, 50, and 100 are presented in Figs. 14(a)–14(c), respectively.

The rescaled vortex convection velocity lies in a broad range of 0.4–1.6 in the near-wall location, such as $y^* \approx 15$. As the wall-normal distance increases, the PDF peak magnitude grows, and the distribution is more concentrated within a narrower and narrower range, which agrees with the study by Gao *et al.* [20]. Meanwhile, the most probable U_c^+ becomes closer and closer to U_m^+, from the largest discrepancy approximately +5%–12% in the buffer layer, then around +2% at $y^* \approx 50$, and finally less than ±1% at $y^* \approx 100$. On the other hand, the mean value lies within 0.98–1.0 times the local U_m^+. In previous works, Wu and Christensen [22] report histograms of the convection velocity of prograde and retrograde vortices, which turns out to be 0.7–1.3 times the local U_m^+ in incompressible channel flows and boundary layers. The present statistics are consistent with their results. Later, Gao *et al.* [20] provide PDFs for the convection velocity of vortex cores and show that the most probable U_c^+ is 0.96–0.98 times the local U_m^+, while the present work recognizes larger ones than U_m^+ in most cases. A likely explanation could be the simple statistical strategy employed

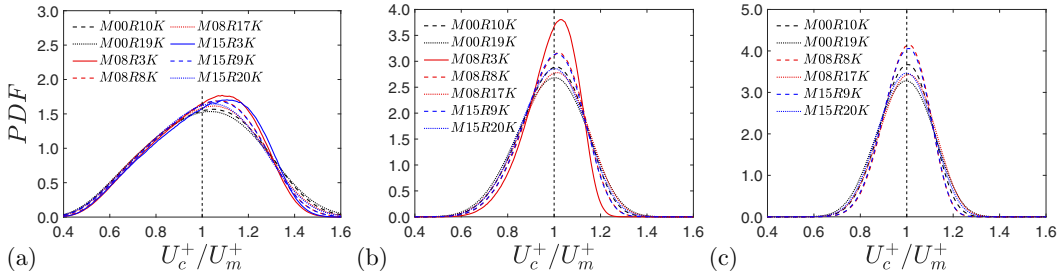

FIG. 14. PDFs of the vortex convection velocity, U_c^+, rescaled by the local mean streamwise velocity, U_m^+, using the DNS database in Table I and the two incompressible cases denoted by the consistent color and line style as defined in Sec. II. The first subfigure presents the statistics at $y^* \approx 15$, the second one at $y^* \approx 50$, and the third one at $y^* \approx 100$.

in this section instead of using the region-growing algorithm to extract vortex cores in Gao *et al.* [20]. This difference may also be attributed to the compressibility effect for the reason that the most probable U_c^+ of incompressible cases obtained from vortex cores are less than one as well, while this observation disappears for compressible cases. In addition, the higher the Re_τ^* is, the closer the most probable U_c^+ becomes to the local U_m^+ for the specific Ma_b and wall-normal location considered.

D. Size and strength of vortices

This subsection investigates the size, strength of vortex cores, and their connection by checking statistics of the vortex core circulation, orientation, and joint PDFs. The evaluation of the vortex radius and circulation has been introduced in Sec. III D. Four cases (Case M08R8K, M08R17K, M15R9K, and M15R20K) in Table I and the two incompressible cases are considered since vortex cores of other cases with lower Re_τ^* are too few to obtain a stable statistical result. The results in Figs. 16 and 17 show perfect collapse among cases with different Re_τ^* and Ma_b. On the contrary, the vortex core radius varies among different cases. Explanations and discussions are presented next.

1. Vortex core radius

The core radius indicates the size of the vortices. Although its PDF varies case by case in Fig. 15, their average radii show a good consistency for all the six cases considered, which is 14–15 at $y^* \approx 15$, 16–18 at $y^* \approx 50$, and 18–19 at $y^* \approx 100$. The mean core radius is increasing for locations further away from the wall. In previous works, Gao *et al.* [20] report that the mean radius is 13.7

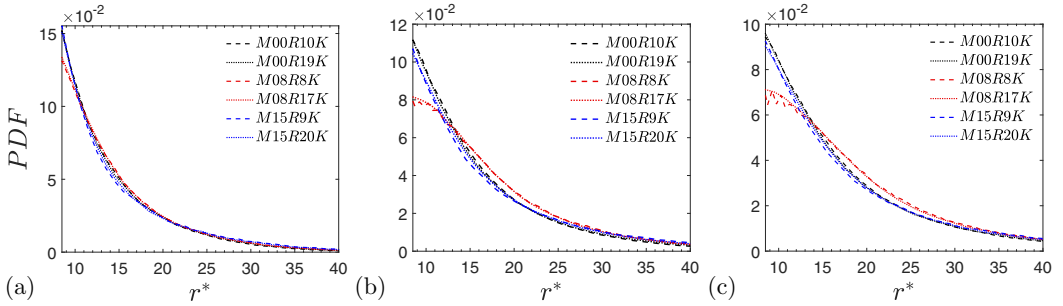

FIG. 15. PDFs of the vortex core radius r^*, using the four DNS cases in Table I and the two incompressible cases denoted by the color and line style as defined in Sec. II. The leftmost subfigure presents the statistics at $y^* \approx 15$, the middle one at $y^* \approx 50$, and the rightmost one at $y^* \approx 100$.

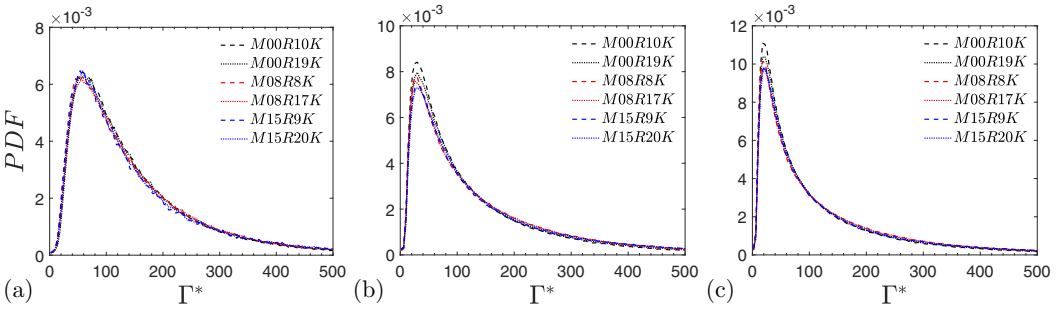

FIG. 16. PDFs of the vortex core circulation Γ^* using the four DNS cases in Table I and the incompressible references denoted by the color and line style as defined in Sec. II. The leftmost subfigure presents the statistics at $y^* \approx 15$, the middle one at $y^* \approx 50$, and the rightmost one at $y^* \approx 100$.

at $y^+ \approx 15$, 14.3 at $y^+ \approx 50$, and 14.6 at $y^+ \approx 100$ in incompressible flows. Carlier and Stanislas [18] observe a slow increase of the mean vortex radius away from the wall from 20 at $y^+ \approx 40$ to 24 in the experiments of incompressible turbulent boundary layers. Pirozzoli *et al.* [19] conclude a comparable vortex size (12–15) in the outer layer. This increasing trend is consistent with previous studies, even though the magnitude varies. The present result is larger than that of Gao *et al.* [20]. The possible reason could be the smaller threshold $\lambda_{ci,\text{thre}}$ in the vortex identification, which is nearly half of that of Gao *et al.* [20] examined using the same incompressible data (M00R19K), and different region-growing algorithms employed.

According to the study by Gao *et al.* [20] and the authors' experience, except for the swirling-strength threshold $\lambda_{ci,\text{thre}}$, PDFs of the core radius are also sensitive to many factors, such as the minimum radius, the angle threshold for the core combination and the threshold of the minimum elevation angle. A factor worth mentioning is the minimum radius, since the vortex cores with smaller radii are ignored, which truncates the PDFs directly. It could be the main reason why the consistency observed in the PDFs of the vortex core circulation and core orientation degenerates for radius.

2. Vortex core circulation

The strength of vortices could be characterized by their circulation Γ^* following the work by Gao *et al.* [20]. Figure 16 shows PDFs of Γ^* at three wall-normal specific locations. A perfect collapse is obtained among compressible and incompressible cases. The most probable circulation is 54–62 at $y^* \approx 15$, 26–34 at $y^* \approx 50$, and 18–22 at $y^* \approx 100$. The PDF moves left with the increasing wall-normal distance, which implies that there are stronger vortices in the buffer layer. The average circulation is 143–147 at $y^* \approx 15$, 124–135 at $y^* \approx 50$, and 111–122 at $y^* \approx 100$. Gao *et al.* [20] report a consistent trend in incompressible flows. However, their results show that PDFs have lower peaks corresponding to stronger circulations, which are 50, 40, and 30 at $y^+ \approx 47$, 110, and 198, respectively. The possible reason might be the same as that discussed in Sec. IV D 1. For instance, a smaller $\lambda_{ci,\text{thre}}$ could lead to a higher population of smaller vortices, which are more likely to be weaker. Hence, the most probable circulation becomes smaller.

A variety of methods to compute the vortex core circulation have been employed in previous studies, such that the magnitude of the vortex circulation differs. Pirozzoli *et al.* [19] determine the core circulation the maximum tangential velocities and core radii at four directions, and then estimate the total vortex circulation (Γ_∞^+) based on the core circulation by the Lamb-Oseen vortex template. In Pirozzoli *et al.* [19], the mean value of Γ_∞^+ increases sharply before $y^+ \approx 20$ and reaches a plateau around 180 in the outer region. Carlier and Stanislas [18] identify vortices based on a detection function indicating the similarity between the selected eddy structure model and the velocity map, and then fit the velocity field with the Oseen vortex model to attain vortex parameters,

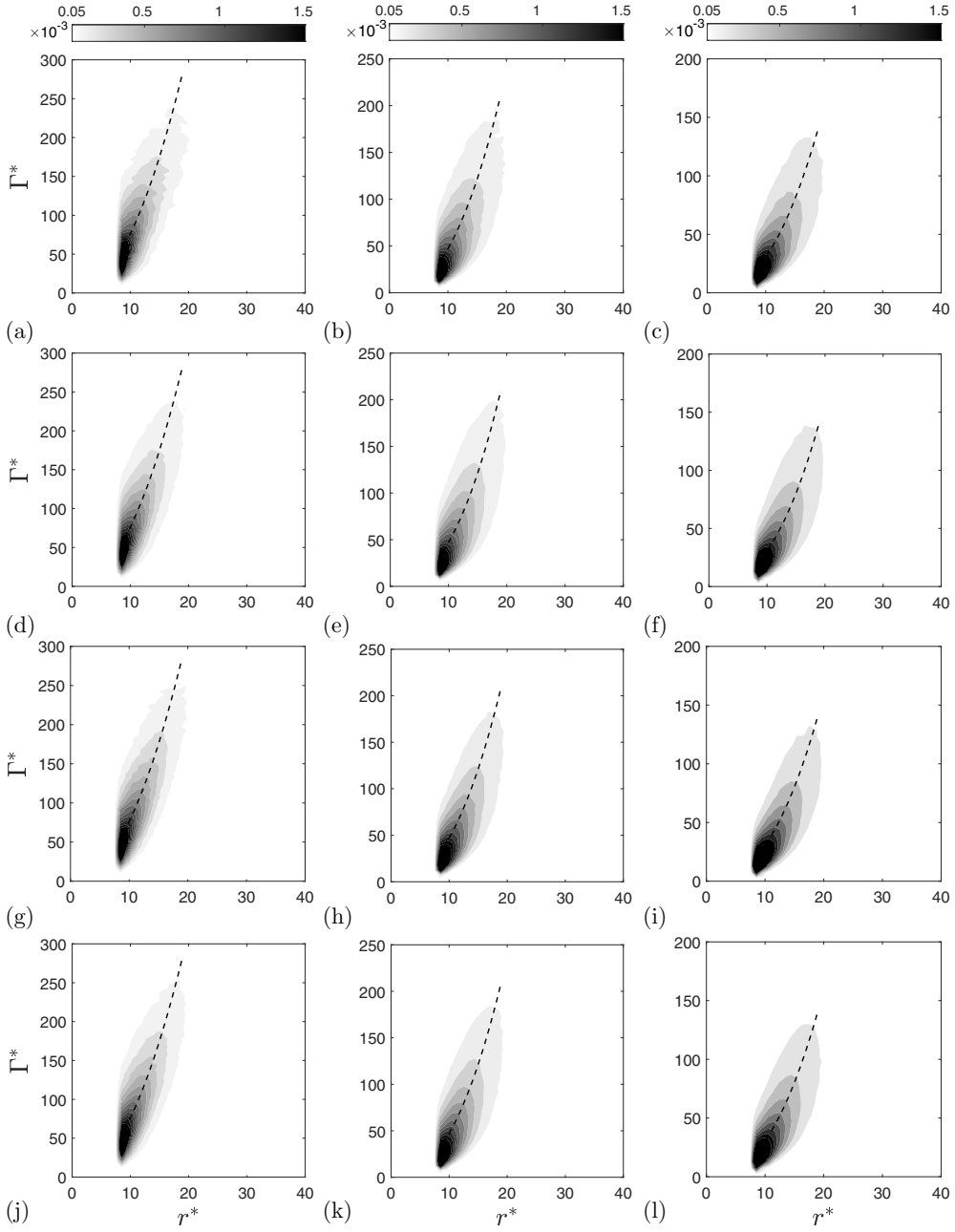

FIG. 17. Joint PDFs of the vortex core radius r^* and circulation Γ^*. The first row presents the statistics from Case M15R9K, the second one from Case M15R20K, the third one from M00R10K, and the last one from Case M00R19K. Joint PDFs at the wall-normal distance $y^* \approx 15$ are shown in the first column, $y^* \approx 50$ in the second one, and $y^* \approx 100$ in the third one. All subfigures share the same color bar. The black dashed line denotes a fitted equation of $|\Gamma^*|$ with respect to r^*: $|\Gamma^*| = 0.68(r^*)^{2.05}$ at $y^* \approx 15$; $|\Gamma^*| = 0.22(r^*)^{2.33}$ at $y^* \approx 50$; $|\Gamma^*| = 0.13(r^*)^{2.38}$ at $y^* \approx 100$.

such as the circulation. They conclude that the vortex circulation remains almost constant from the top of the buffer layer ($y^+ = 50$) to the middle of the logarithmic region, which is consistent with the result of Pirozzoli *et al.* [19]. Generally, a comparable vortex strength could be observed in the logarithmic region considered in this work.

3. Interrelation of the vortex size and strength

Having discussed the size and strength of vortices, it is now necessary to reveal the interrelation of these two parameters. To explore it, joint PDFs are provided as follows. In order to be concise, the joint PDFs of cases M08R8K and M08R17K are not presented, as they give similar results to other cases.

Joint PDFs of the core circulation and radius are plotted in Fig. 17. A good agreement between the compressible and incompressible cases can be observed. A power-law function $|\Gamma^*| = a(r^*)^b$ is also superposed, where a and b are parameters fitted by the corresponding most probable radius for a specific circulation using the least-squares method. The explicit expression can be found in the caption of Fig. 17. As proposed by Gao *et al.* [20], $b > 2$ indicates that the larger the vortex core is, the stronger its average vorticity is, because the circulation is estimated by the integration of vorticity over the core's in-plane area. The other parameter a implies the mean magnitude of the local vorticity. Gao *et al.* [20] declare a slightly increasing trend of parameter b from 2.1 ($y^+ \approx 47$) to 2.2 ($y^+ \approx 110$ and 198) and a decreasing trend of parameter a from 0.51 ($y^+ \approx 47$) and then 0.34 ($y^+ \approx 110$) to 0.26 ($y^+ \approx 198$) in incompressible channel flows. The same patterns of parameters a and b are observed in the present work as well. Specifically, the parameter b in both the buffer layer and the logarithmic region is larger than 2 and grows from 2.05 ($y^* \approx 15$) to 2.33 at $y^* \approx 50$ and finally 2.38 at $y^* \approx 100$. Starting from 0.68 at $y^* \approx 15$, the parameter a declines sharply to 0.22 at $y^* \approx 50$, and then 0.13 at $y^* \approx 100$. Gao *et al.* [20] argue that the decrease of the parameter a is due to the shrinking of the mean magnitude of vorticity with wall-normal distance, as observed by Stanislas *et al.* [58]. Despite the fact that parameters a and b have a different magnitude from that in the paper [20], it is acceptable to conclude the consistency between the compressible and incompressible channel flow explored in the present work and the incompressible channel flow in Gao *et al.* [20].

4. Morkovin's hypothesis and semilocal units for instantaneous vortex features

As discussed in Sec. IV B 3, the evolution of vorticity in compressible flows primarily relies on vortex stretching and viscous diffusion for the present data with Ma < 1.5, which share the same mechanism as incompressible flows [57]. However, the magnitude could be significantly different. For instance, though Sec. IV B verifies the stretching direction stays unchanged, the stretching strength may vary. Additionally, the viscosity coefficient changes due to the variation in temperature. These instantaneous vortex features, i.e., radii and circulation, are the combined effects of the vortex stretching and the viscous diffusion. If an agreement for them can be achieved, then one needs a certain rescaling that compensates for these variations, such as the streamwise velocity transformation which requires a rescaling not only for the wall-normal coordinate by mean flow properties but also for the mean velocity itself.

One potential choice is the semilocal units deduced from Morkovin's hypothesis [26], accounting for the compressibility effect by the variation of mean flow properties at moderate Mach numbers. The semilocal scaling succeeds in many mean statistics, e.g., mean velocity profiles and profiles of the Reynolds stress. Whether Morkovin's hypothesis and semilocal units can be extended to these instantaneous features is still a question. The previous sections show that the vortex radius and circulation in compressible flows collapse to their counterparts in incompressible flows by employing semilocal scaling. Thus, Morkovin's hypothesis and semilocal units are also applicable to instantaneous vortex features, at least for Mach numbers included in this work.

E. Vortex population

The population trends of prograde, retrograde, and streamwise vortices and the total number are investigated in this subsection. Prograde spanwise vortices rotate in the same direction as the mean shear, while retrograde spanwise vortices are in the opposite direction. In the present study, those vortex cores with $|\theta_{-zx,c}| \leqslant 10^\circ$ are considered as prograde vortices, $|\theta_{-zx,c}| \geqslant 170^\circ$ as retrograde vortices, and $80^\circ \leqslant |\theta_{-zx,c}| \leqslant 100^\circ$ as streamwise vortices, since based on the ideal hairpin vortex model, the rotation and stretching directions form an acute angle in most cases.

The population distribution can be a function with respect to the wall-normal distance, Reynolds number, and Mach number for compressible turbulent channel flows. The population density $\Pi(y/h)$ is defined as the ensemble-averaged number of vortices N divided by the corresponding statistical area they reside in. Here a subscript is employed to denote the type of vortices, i.e., p for prograde spanwise vortices, r for retrograde vortices, s for streamwise vortices, and T for the total number of all kinds of vortices. For instance, the number density of prograde vortices $\Pi_p(y/h)$ is given by

$$\Pi_p(y/h) = \frac{N_p(y/h)}{\frac{L_x}{h}\frac{L_z}{h}}, \tag{7}$$

where L_x and L_z are the size of the statistical region in the x and z directions, respectively. This equation indicates the number of prograde vortices in the area of h^2 for a specific wall-normal location y/h, which is the outer-scaled number density. Alternatively, the semilocal-scaled number density of prograde vortices $\Pi_p^*(y^*)$ is given by

$$\Pi_p^*(y^*) = \frac{N_p(y^*)}{L_x^* L_z^*}, \tag{8}$$

where L_x^* and L_z^* are the size of the statistical region in the semilocal scaling. $\Pi_p^*(y^*)$ represents the number density of prograde vortices in the area of δ_τ^{*2} at a specific y^*.

The outer-scaled and semi-local-scaled number densities versus y/h and y^* are shown in Fig. 18. For the outer-scaled number density, the effect of Re_τ^* is more distinct, while Ma_b has less influence. All the four number densities from cases with a higher Re_τ^* are much larger. Π_p has a peak in the near-wall region ($y/h < 0.2$), then decreases monotonically with y/h for all cases examined. Wu and Christensen [22] also report this rise-fall trend of Π_p in incompressible channel flows and boundary layers. For retrograde vortices, Π_r has two local maxima, the first local maximum at $y/h \approx 0.2$ and the second one at the center line of the channel ($y/h \approx 1$). Wu and Christensen [22] notice a similar trend in incompressible channel flows, while the number density of retrograde vortex in incompressible boundary layers maintains decreasing after the first peak. The reason could be that part of retrograde vortices originate from the flow near the opposite wall, as argued by Wu and Christensen [22]. These retrograde vortices are equivalently prograde in the reference frame of the opposite wall, and they advect across the center line and join the flow near the bottom wall. Similar to Π_p, the other two types of number densities Π_s and Π_T achieve their maxima within $y/h < 0.2$.

Compared with the outer-scaled number density, the semi-local-scaled counterpart is shown in Figs. 18(b)–18(h), whose variation with respect to y^* collapses better in the near wall region. The rise-fall pattern mentioned above is also observed for Π_p^*, Π_s^*, and Π_T^*. Π_p^* approaches its peak at about $80 < y^* < 90$, while Π_s^* and Π_T^* early at $y^* \approx 40$ and $y^* \approx 70$, respectively. Again, Π_r^* has two peaks, whose reason has already been discussed above. For the first peak, the four high-Re_τ^* cases approach it at around $y^* \approx 130$, and the two low-Re_τ^* compressible cases at $y^* \approx 120$ corresponding to $y/h \approx 0.3$ the outer edge of the logarithmic region. The explanation could be that the logarithmic region of the two low-Re_τ^* cases is too short to reach the same peak as the high-Re_τ^* cases. Additionally, the first peak is followed by a slight reduction such that its magnitude is lower while achieved at a smaller y^*.

The population distribution is further explored by the proportion Ψ of different kinds of vortices to the total number and its variation in the wall-normal direction. The same subscript is employed to distinguish different types of vortices as mentioned above, e.g., the fraction of prograde vortices

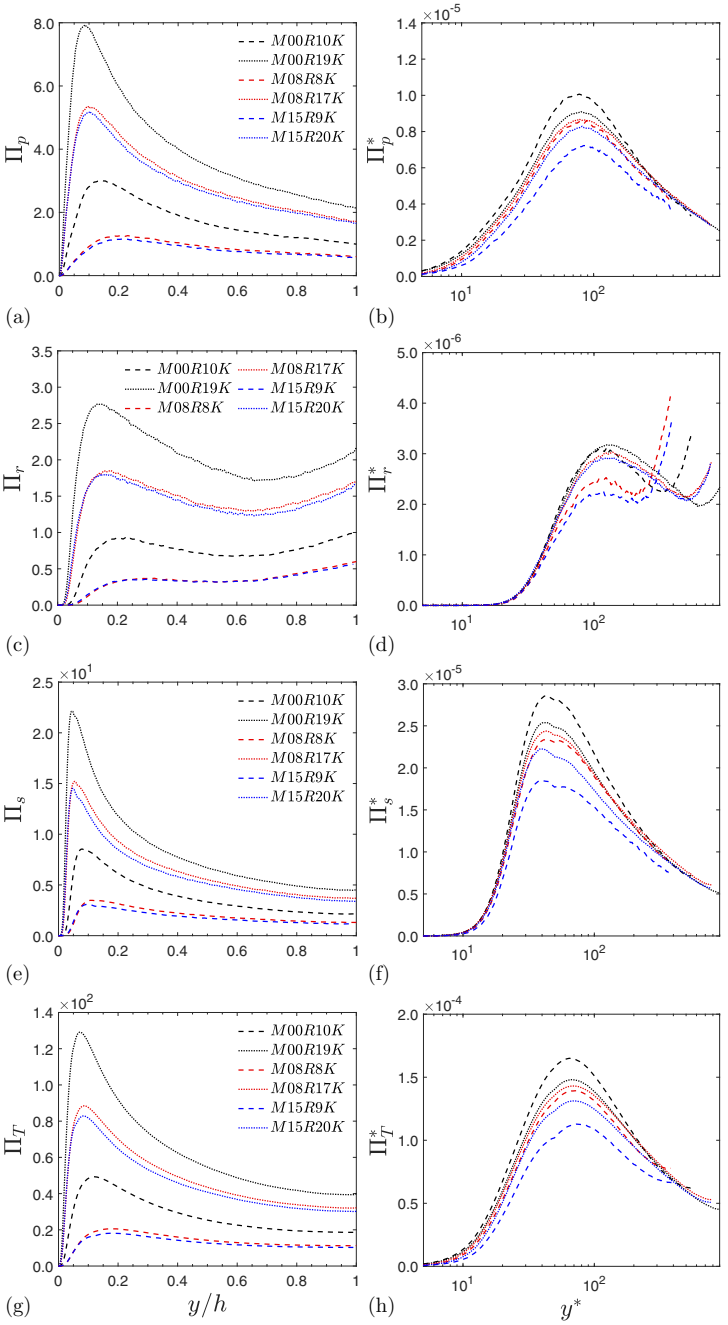

FIG. 18. The outer-scaled population density distributions of prograde (Π_p), retrograde (Π_r), streamwise (Π_s) vortices, and the total vortices (Π_T) with respect to y/h are shown in (a), (c), (e), and (g), respectively. The semilocal-scaled population density distributions of prograde (Π_p^*), retrograde (Π_r^*), streamwise (Π_s^*) vortices and the total vortices (Π_T^*) with respect to y^* are shown in (b), (d), (f), and (h), respectively.

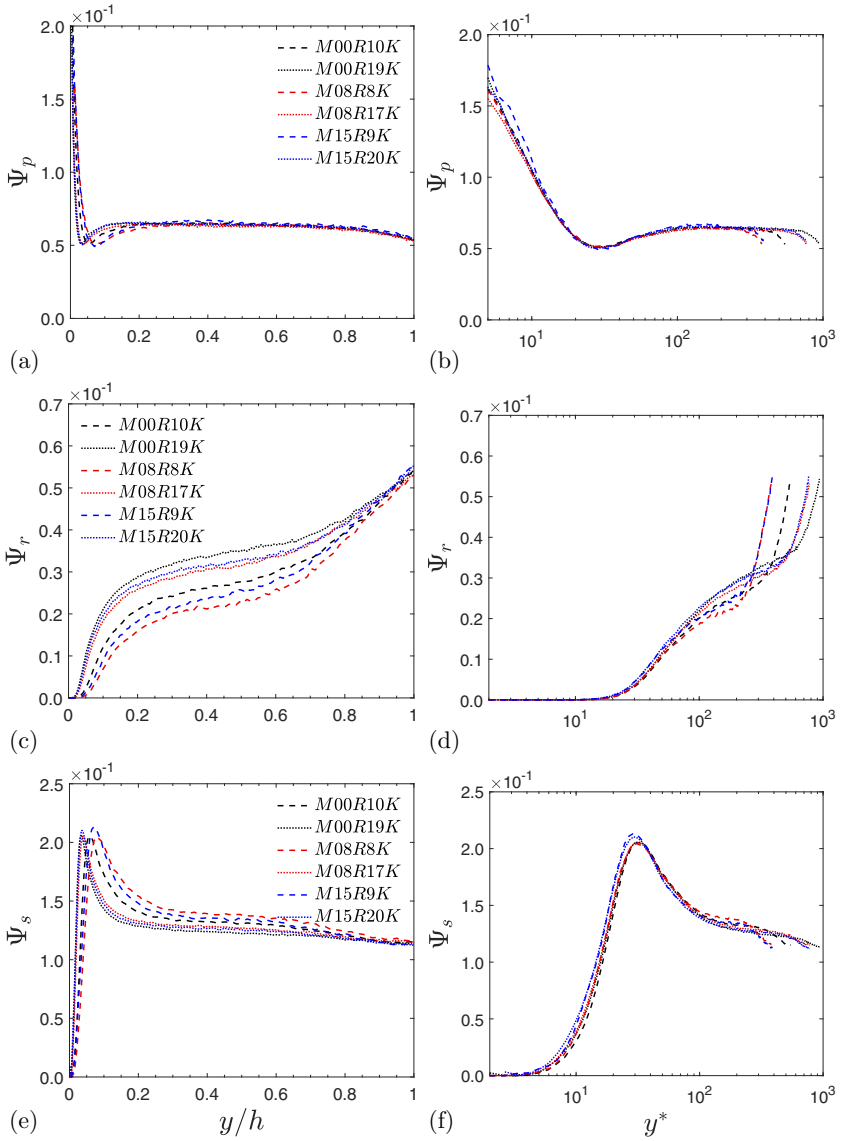

FIG. 19. The fraction distributions of prograde (Ψ_p), retrograde (Ψ_r), and streamwise (Ψ_s) vortices with respect to y/h are shown in (a), (c), and (e), respectively; those with respect to y^* are shown in (b), (d), and (f), respectively.

Ψ_p for a specific wall-normal location y is defined as

$$\Psi_p(y) = \frac{\Pi_p(y)}{\Pi_T(y)}. \tag{9}$$

Figure 19 displays fractions of three kinds of vortex versus y/h and y^*. For Ψ with respect to y/h [see Figs. 19(a), 19(c), and 19(e)], an overall collapse among cases can be seen only near the center line, while a more consistent collapse among cases examined can be seen in the semilocal scaling [see Figs. 19(b), 19(d), and 19(f)] in the near-wall region. The peak of Ψ_p is in the viscous sublayer, and it keeps reducing in the buffer layer until the inner edge of the logarithmic region. A

slight rise can be found at the beginning of the logarithmic region, and then it levels off. There are almost no retrograde spanwise and streamwise vortices in the viscous sublayer, where Ψ_r and Ψ_s are approximately zero. Ψ_r begins to increase from the middle of the buffer layer and a more steep increment is noticed from $y/h \approx 0.7$. With respect to Ψ_s, it starts growing in the buffer layer, approaches its peak at $y^* \approx 30$ followed by a reduction to $y^* \approx 50$, and ultimately levels off within the logarithmic region. To further determine the dominant structures, the ratio of the number densities of prograde and retrograde spanwise cores and streamwise cores, i.e., $\Pi_p : \Pi_r : \Pi_s$, is investigated quantitatively. At $y^* \approx 15$, $\Pi_p : \Pi_r : \Pi_s$ is approximately 2:0:3. In the logarithmic region, the ratio becomes 4.5:1:13 for $y^* \approx 50$, 3:1:6.5 for $y^* \approx 100$, and 2.5:1:5.3 for $y^* \approx 150$. In the outer layer ($y/h \approx 0.5$), this ratio is 2:1:4 based on the high-Re_τ^* cases. In summary, streamwise and prograde vortices are comparable in the buffer layer. Then, the number of streamwise vortices rises sharply until the inner edge of the logarithmic region, after which both prograde and retrograde spanwise vortices appear more and more frequently with the increasing wall-normal distance.

F. Further discussions

In the discussion above, we uncover some characteristics of vortices using Eq. (3) considering the close association between vortex structure and vorticity. Obviously, the mechanism becomes far more complex in high-Mach compressible flows. Equation (3) has extra terms compared with its form in incompressible flows, including the compressibility effect (the first term on the right-hand side), the baroclinic torque (the third term) and the torque generated by the variation of shear stress and density (the fourth term). In addition, the strength variation of strain and the variation of viscosity also take effect. It is concluded that these extra terms are negligible for all the cases included here, and the governing mechanism for vorticity evolution and vortex evolution is similar to incompressible flows. Besides, the semilocal scaling compensates for the variation of flow properties such that good consistency is achieved for instantaneous vortex features among channel flows with Mach numbers from 0 to 4. However, these effects may be more and more dominant as the Mach number increases. Although the range of Mach and Reynolds numbers in our channel flow database almost represents the state-of-the-art in the literature, it is still not rigorous to confirm the validity for very high Mach numbers due to the lack of databases. To comprehensively study the compressibility effects with a more critical parameter range on this topic is rather essential and belongs to our future work when the new databases are available.

Another aspect of interest in compressible flows is the shock wave. According to Crocco's theorem [59], the curved shock generates vorticity by inducing nonuniform entropy downstream. Their interaction with vortices could be even more sophisticated, which is another active research topic. Both the shock and vortex deform during the interaction. The shock waves compress vortices in the streamwise direction, e.g., a circular vortex can become an elliptical one after a shock [60]. Meanwhile, strong vortices diffract and reflect shock waves, which is closely related to the generation of acoustic waves. In the cases used in the present work, however, we have not noticed the existence of shocks, and nor have them been observed by researchers in turbulent boundary layers with Mach number smaller than 10 [61,62]. Thus, the study of these phenomena is out of the scope of this work.

Though the present work concentrates on compressible channel flows, one could extrapolate the obtained conclusions to other types of compressible wall turbulence, like pipe flows and boundary layers. Considering the similarity of turbulent channel flows and pipe flows throughout the inner and outer layer [63], all the findings above stand a high opportunity to be established in compressible pipe flows. In regard to compressible boundary layers, the difference compared with pipe or channel flows originates from the large-scale energetic motions in the outer regions [63]. Characteristics of vortices might mostly remain similar in the near-wall region. On the other hand, in the outer region, some properties may still hold, e.g., $\theta_{xy,m}$ still approaches 45° based on our theoretical analysis above. Some observations may disappear, like the increase of retrograde vortices near the center line. Since the main difference can be attributed to very large-scale motions or superstructures that

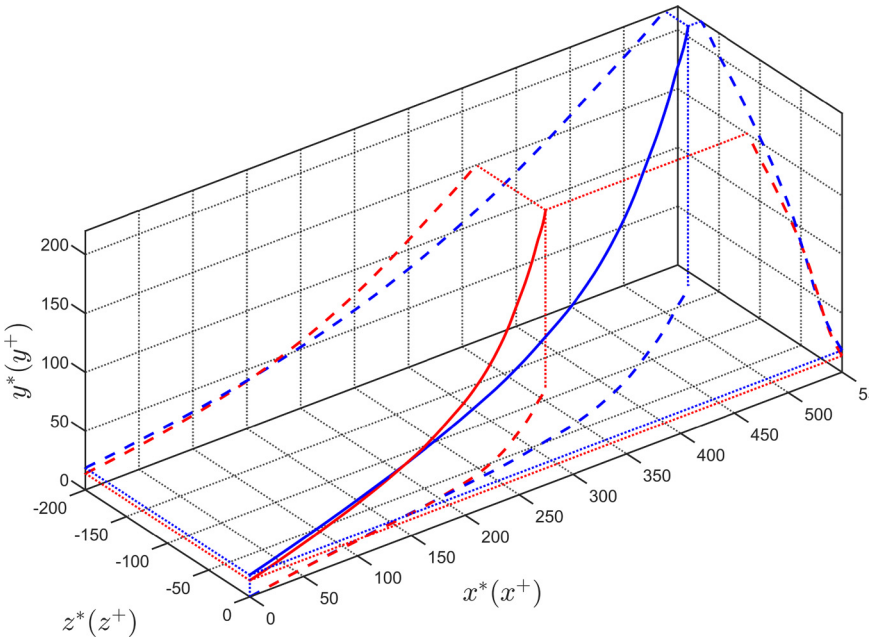

FIG. 20. A sketch for the topology of dominant vortex structures from $y^* \approx 14$ to 150 ($y^+ \approx 18$ to 220). The red lines represent the model in the semilocal scaling, and the blue lines represent that in the wall unit. The solid lines represent the 3D vortex filament. Their projections onto the x-y, z-x, and y-z planes are shown by the dashed lines. The dotted lines indicate the projection lines.

are not directly associated with vortex structures, concluding the distinction and similarity of more characteristics, such as the vortex size and strength, requires further studies.

G. A sketch of vortex tube based on statistics

This section is dedicated to providing a quantitative heuristic model for the topology of vortex structures. It is an improvement beyond the classical conceptual hairpin vortex model, whose features remain qualitative. In order to characterize its geometry, the present work neglects its thickness as a vortex filament.

This 3D model is given by the following differential equations:

$$\frac{dx_f}{dy_f} = \cot(\theta_{xy,m}), \tag{10}$$

$$\frac{dz_f}{dx_f} = -\cot(\theta_{-zx,m}). \tag{11}$$

By manipulating Eqs. (10) and (11), the relation between dz_f and dy_f is obtained as

$$\frac{dz_f}{dy_f} = -\cot(\theta_{-zx,m})\cot(\theta_{xy,m}), \tag{12}$$

where x_f, y_f, and z_f denote the coordinates of the vortex filament in the x, y, and z directions, respectively. Then, one can obtain the topological shape of the vortex filament as shown in Fig. 20 by an integration of Eqs. (10) and (12). $\theta_{xy,m}$ and $\theta_{-zx,m}$ are the most probable inclination angles from PDFs in Sec. IV B 1 varying with y^*. In this subsection, only the result from Case M15R20K is used, which has the highest Ma_b and Re^*_τ, and the finest spatial resolution.

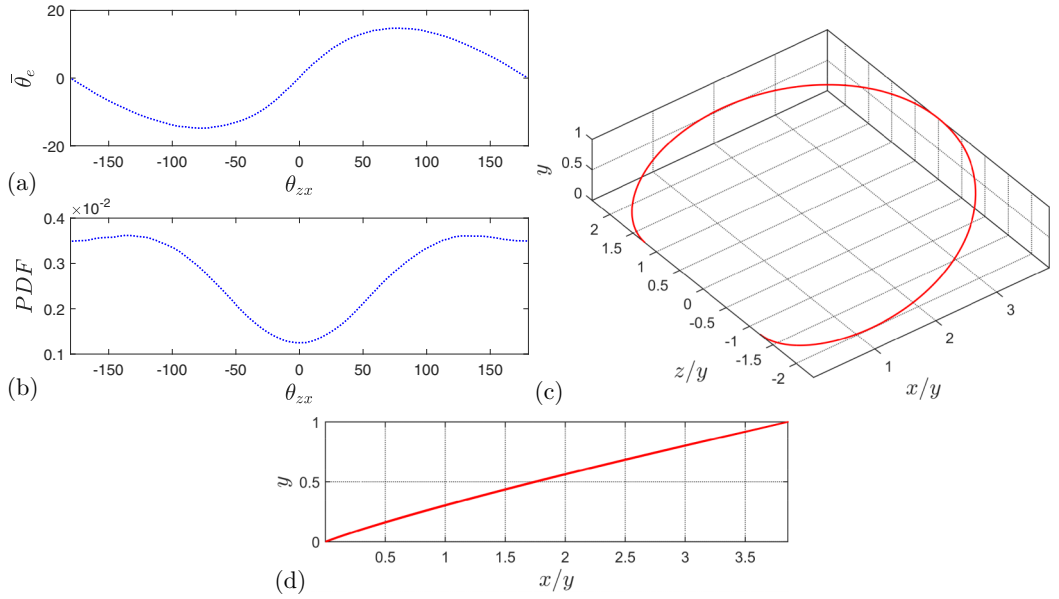

FIG. 21. The replication of the topology vortex model in Pirozzoli *et al.* [19] and corresponding angle distributions computed at $y/h = 0.5$ using case M15R20K. (a) The approximately sinusoidal dependence of $\overline{\theta}_e$ on θ_{zx}; (b) the PDF of θ_{zx}; (c) the 3D view of the vortex model with its height normalized to be one; and (d) its projection onto the x-y plane.

Due to the symmetric patterns of θ_{xy} and θ_{-zx}, the PDF within the range of $0^\circ < \theta_{xy}, \theta_{-zx} < 180^\circ$ are employed. The interval of integration is 14–150 semilocal units (corresponding to 18–220 in the wall unit). The 3D curves in both the wall unit and the semilocal scaling (blue and red solid lines) and their orthogonal projections on the x-y, z-x, and y-z planes (blue and red dashed lines) are displayed in Fig. 20. An apparent difference is noticed for the same vortex filament in these two scales. According to the structural similarity established above, the one in the semilocal scaling is more appropriate, and we will concentrate on it. The red curve is similar to the one in Wang *et al.* [21] for incompressible turbulent boundary layers. A more and more steep upward bending shows up in the x-y plane, indicating that a larger and larger inclination angle forms between the dominant vortex structure and the wall. Consistent with incompressible cases, an Ω shape corresponding to the hairpin leg appears in the y-z plane. For $y^* > 50$, the direction of the vortex filament changes from streamwise to quasispanwise, which is more obvious in the y-z plane than in the z-x plane. The current model shows a satisfactory agreement with the classic hairpin vortex model and the vortical structures extracted from the instantaneous λ_{ci} field in Figs. 6(a) and 7(a).

To clarify the advantages and weaknesses of this model requires a comparison with other topology models in prior studies: the ringlike one for compressible flows in Pirozzoli *et al.* [19] and an analogous one for incompressible flows in Wang *et al.* [21]. Although they all rely on the differential equation and integration, each has its own concentration and assumption. Pirozzoli *et al.* [19] notice that the conditional expected value of θ_e depends on θ_{zx} sinusoidally as shown in Fig. 21(a), which can be interpreted by a closed-loop vortex filament. θ_e is the elevation angle formed with the wall, and θ_{zx} has a similar definition to θ_{-zx} defined in Fig. 4 but represents the one formed with z direction. They consider a differential equation of the vortex filament with respect to the arc length s [see Eqs. (4.7) and (4.8) in their work] and assume that (i) the conditional expected value $\overline{\theta}_e$ is a function of θ_{zx} in the outer region and (ii) the differential arc length is estimated by the probability of the associated θ_{zx}, i.e., $ds \sim P(\theta_{zx})d\theta_{zx}$, where $P(\theta_{zx})$ denotes the corresponding PDF.

The integration of $P(\theta_{zx})$ from $-\pi$ to π gives a ringlike topology. We replicate their calculations and show results in Fig. 21. The sinusoidal dependence of $\overline{\theta}_e$ on θ_{zx} observed at $y/h = 0.5$ in Figs. 21(a), and 21(b) provides the PDF of θ_{zx}. Although we do not obtain a closed loop in Fig. 21(c), the topology has an acceptable ringlike shape. One possible reason for this discrepancy is that this work uses the real eigenvector to characterize the vortex orientation instead of the vorticity vector in Pirozzoli *et al.* [19]. In addition, this work adopts the total velocity gradient tensor while Pirozzoli *et al.* [19] employ the fluctuating velocity gradient tensor. Both these two factors alter the PDF of θ_{zx}, especially the region near $\theta_{zx} = 0/\pm 180$, which ultimately result in the unclosed loop in Fig. 21(c). As one can expect, the method in Pirozzoli *et al.* [19] focuses on vortex structures in the outer region, while the present model is more in the buffer layer and the logarithmic region. Based on the noted relation between $\overline{\theta}_e$ and θ_{zx}, it can provide a reasonable topology in the outer region using statistics from only one wall-normal location, unlike the current one which has to use multiple wall-normal locations. However, it might deviate from instantaneous structures since the conditional expected value $\overline{\theta}_e$ could be an assemblage effect of multiscale vortices. This point is clearly demonstrated by its projection on the x-y plane in Fig. 21(d), which has a much smaller inclination angle around 15° than the theoretically estimated 45° [55,64]. Comparably, the model in Wang *et al.* [21] and the present model could reflect the instantaneous structures better since the most probable angles are adopted.

In regard to the model in Wang *et al.* [21], the fitting step for the most probable angle using a second-order polynomial is ignored because the raw data without fitting can provide a smooth topology in the present work. We extend this model to compressible flows by applying the semilocal scaling in the wall-normal direction. This topology is uniform at least for Re_τ^* and Ma_b examined in this work, due to the consistency among all the compressible and incompressible cases. One weakness merits mentioning that the current model is deduced under the assumption that the most probable angle varying with $y^*(y^+)$ is obtained from one vortex extending in the wall-normal direction. Actually, the most probable angle at different $y^*(y^+)$ may come from vortices of multiple scales. Considering this aspect, the current model is more likely to be an assembly of pieces from multiscale vortices (the assemblage effect should be much weaker than the model in Ref. [19]). Overall, this model could perform as a reliable vortex topology while using vortex methods to compute flow fields.

V. CONCLUDING REMARKS

The present work utilizes DNS databases of compressible channel flows with Ma_b up to 4 to explore the statistical features of vortex structures, including their orientations, convection velocities, sizes, strength, and population tendencies.

The vortex orientation characterized by the real eigenvector depends less on Ma_b and Re_τ^* if the wall-normal distance is scaled by the semilocal scaling. Both theoretical estimation and statistical results show an increasing trend towards 45° of the inclination angle θ_{xy} with y^* increases. A heuristic model representing instantaneous vertical structures is proposed based on the most probable angles. Meanwhile, the most probable θ_{-zx} reduces with y^*, and $\theta_{-zx} = 0°$ occurs more frequently. For vortex cores, their average size r^* and strength Γ^* in the semilocal scaling are consistent for all the cases considered. Even though a slight growth of the average r^* is observed with increasing y^*, the average Γ^* turns out to be weaker and weaker.

Vortices on average, advect at the local mean streamwise velocity. The distribution of the vortex convection velocity U_c^+ becomes narrower and narrower with increasing y^*, and so does the discrepancy between the most probable U_c^+ and U_m^+.

The population of prograde, retrograde, and spanwise vortices and the total population are investigated. Both inner- and semi-local-scaled number densities show an obvious dependence on the Reynolds number and marginal dependence on the Mach number, but their fractions have a satisfactory collapse versus y^*. Except for retrograde vortices, populations of the other three types reach their peak in the logarithmic region. The number of prograde and streamwise vortices is

comparable at $y^* \approx 15$. Then, streamwise vortices gradually dominate near the inner edge of the logarithmic region, after which the fraction of spanwise vortices grows continuously over the entire outer layer.

This work provides a relatively comprehensive study of the kinematic properties of vortical structures in compressible channel flows. Overall, a quantitative consistency of most features between compressible and incompressible channel flows after applying the semilocal scaling is observed. This indicates that Morkovin's hypothesis is valid not only for mean flow variable statistics but for the instantaneous vortex features as well. It is a piece of crucial knowledge for developing advanced modeling approaches [29] and extending incompressible theories and models to compressible flows. It also shows that the principal mechanism (vortex stretching and viscous diffusion) dominating the vortex evolution remains unchanged through analyzing the vorticity evolution equation. The compressibility effect and attendant torques are negligible at moderate Mach numbers considered here. To concretely validate this point, another aspect of interest, their dynamic properties, requires more investigation as well. These statistics themselves are also of importance. Mean values and distributions, as well as the topological model, provide a fundamental reference if one intends to reconstruct the flow field by pilling up vortices of various scales. In addition, corresponding studies regarding vortical features in the hypersonic channel flows and boundary layer and the influence of wall temperature are still lacking. Thus, future studies are recommended to give a comprehensive insight into vortices in the compressible wall turbulence.

ACKNOWLEDGMENTS

L.F. acknowledges the open fund from State Key Laboratory of High-Temperature Gas Dynamics, LHD (No. 2021KF03), the fund from the Research Grants Council (RGC) of the Government of Hong Kong Special Administrative Region (HKSAR) with RGC/ECS Project (No. 26200222) and RGC/GRF Project (No. 16201023), and the fund from the Project of Hetao Shenzhen-Hong Kong Science and Technology Innovation Cooperation Zone (No. HZQB-KCZYB-2020083). X.L. acknowledges the fund from NSFC Project (No. 12232018). This work is also partially supported by the Research Grants Council (RGC) of the Government of Hong Kong Special Administrative Region (HKSAR) with RGC/STG Project (No. STG2/E-605/23-N).

The authors report no conflict of interest.

APPENDIX A: VALIDATION OF DNS DATABASES

DNSs of compressible turbulent channel flows have been conducted with a finite-difference code, by solving the 3D unsteady compressible Navier-Stokes equations. The convective terms are discretized with a seventh-order upwind-biased scheme, and the viscous terms are evaluated with an eighth-order central difference scheme. Time advancement is performed using the third-order strong-stability-preserving Runge-Kutta method [65]. A constant molecular Prandtl number Pr of 0.72 and a specific heat ratio γ of 1.4 are employed. The dependence of dynamical viscosity μ on temperature T is given by Sutherland's law, i.e.,

$$\mu = \mu_0 \frac{T_0 + S}{T + S} \left(\frac{T}{T_0} \right)^{3/2}, \tag{A1}$$

where $S = 110.4$ K and $T_0 = 273.1$ K.

All the DNSs are carried out in a rectangular box with the given sizes along streamwise, spanwise, and wall-normal directions, respectively. In the streamwise and spanwise directions, the mesh is uniformly spaced, whereas, in the wall-normal direction, the mesh is hyperbolically clustered towards the walls. The isothermal no-slip conditions are imposed at the top and bottom walls, and the periodic boundary condition is imposed in the wall-parallel directions, i.e., x and z directions. All simulations begin with a parabolic velocity profile with random perturbations superimposed and uniform temperature and density values. A body force is imposed in the streamwise direction to

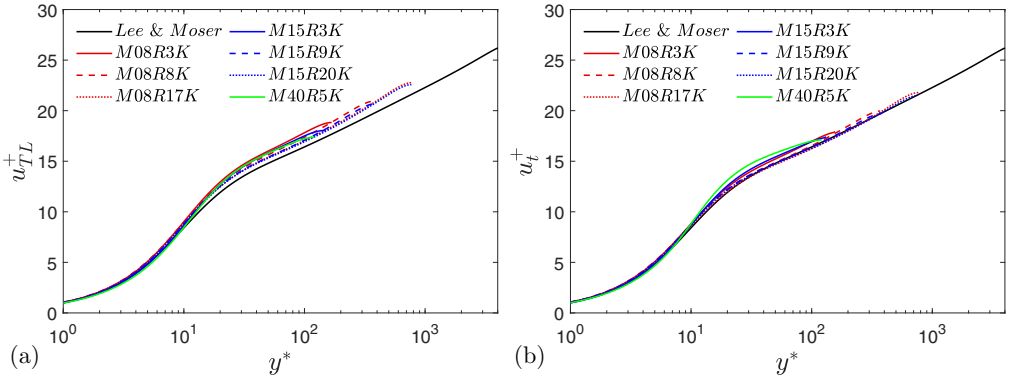

FIG. 22. Mean streamwise velocity profiles transformed by (a) the Trettel-Larsson transformation [28] and (b) the total-stress-based transformation [29]. All the DNS cases in Table I are examined. The black solid line denotes the reference and is taken from the incompressible channel flow with $\mathrm{Re}_\tau \approx 5200$ in Ref. [70].

maintain a constant mass flow rate, and a corresponding source term is also added to the energy equation. The code has been validated by previous studies on the energy-containing eddies in subsonic channel flows [66] and supersonic channel flows [67–69].

The accuracy of the DNS database in Table I is examined using the mean streamwise velocity profile and the semi-local-scaled Reynolds normal stress. Due to the compressibility effect, a velocity transformation is required for the compressible wall-bounded turbulence to recover the universal law-of-the-wall in incompressible flows. The Trettel-Larsson [28] and total-stress-based [29] transformations are employed in this work since they have been widely recognized as effective methods for compressible channel flows. The transformed velocity profiles are shown in Fig. 22(a) for the Trettel-Larsson transformation [28] and (b) the total-stress-based one [29]. All the cases show a satisfactory collapse to the well-known law-of-the-wall, and the performance of the total-stress-based transformation [29] is even better.

For the six cases in Table I, three semi-local-scaled Reynolds normal stress components $\tau_{ii}^* = \overline{\rho}\widetilde{u_i''u_i''}/\tau_w$, where $i = 1$, 2, and 3, are examined in Fig. 23. Cases of M08R3K, M08R3K, M08R17K, and M15R3K [see Figs. 23(a)–23(c) and 23(e)] share the same Ma_b and Re_b with the data of compressible channel flows by Yao and Hussain [71] and a decent agreement can be found. The other two cases, M15R9K and M15R9K [see Figs. 23(d) and 23(f)], are compared with the data of compressible channel flows by Modesti and Pirozzoli [72] with similar Re_τ and Ma_b. An acceptable consistency can be observed, although a narrow discrepancy exists due to the slight difference of Re_τ. As for the case M40R5K, there is no existing data sharing similar Ma_b and Re_b for a fair comparison. Therefore, its stress components are not presented. Overall, the accuracy of the present data set in Table I has been verified.

APPENDIX B: ADAPTABILITY OF PARAMETER η

This section validates the adaptability of η used to estimate the threshold for λ_{ci}. The range of η considered is from 0.2 to 0.4, and the corresponding threshold is from $\lambda_{ci,\mathrm{thre}} = 0.2/\mathrm{PDF}_{\max}$ to $\lambda_{ci,\mathrm{thre}} = 0.4/\mathrm{PDF}_{\max}$. We compare the threshold determined in Sec. III A with two bounds of the interval to reveal its impact on the vortex orientation, size, and strength, using two representative cases: M00R19K and M15R20K. The validation begins with the vortex orientation shown in Fig. 24. Obviously, the shape of PDFs of θ_{xy}, θ_{-zx} remains similar with different choices of η. Figure 25 demonstrates the variation of vortex radii with η. A higher probability density appears at smaller radii at $y^* \approx 15$ as η decreases. Conversely, in the logarithmic region, smaller radii are more likely to appear as η increases. Since these changes in PDFs are slight, the mean vortex radius has a

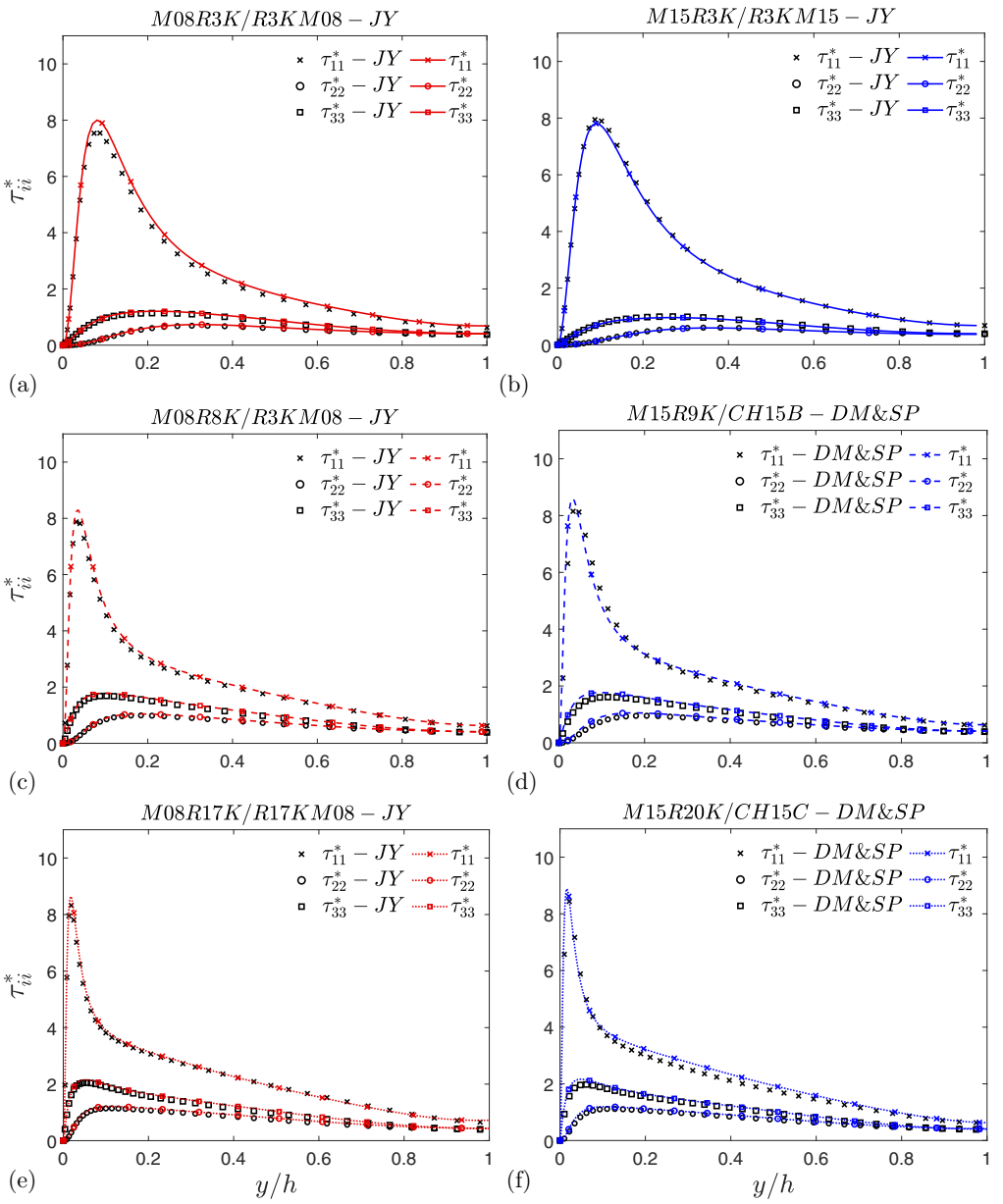

FIG. 23. Distributions of the Reynolds normal stress components τ_{ii}^*, $i = 1$, 2, and 3, with respect to y/h for six DNS cases in Table I, which are compared with the data of corresponding compressible channel flows in Refs. [71] and [72] denoted by the same case name as original papers.

slight decline, around 10%, and the rising tendency of radii still exists. The variation of vortex strength is more consistent for different wall-normal locations as indicated by Fig. 26. When η becomes smaller, distributions of the vortex strength tend to move leftward and vice versa. The resultant mean circulations vary around 10%, which does not alter the conclusion of the present work.

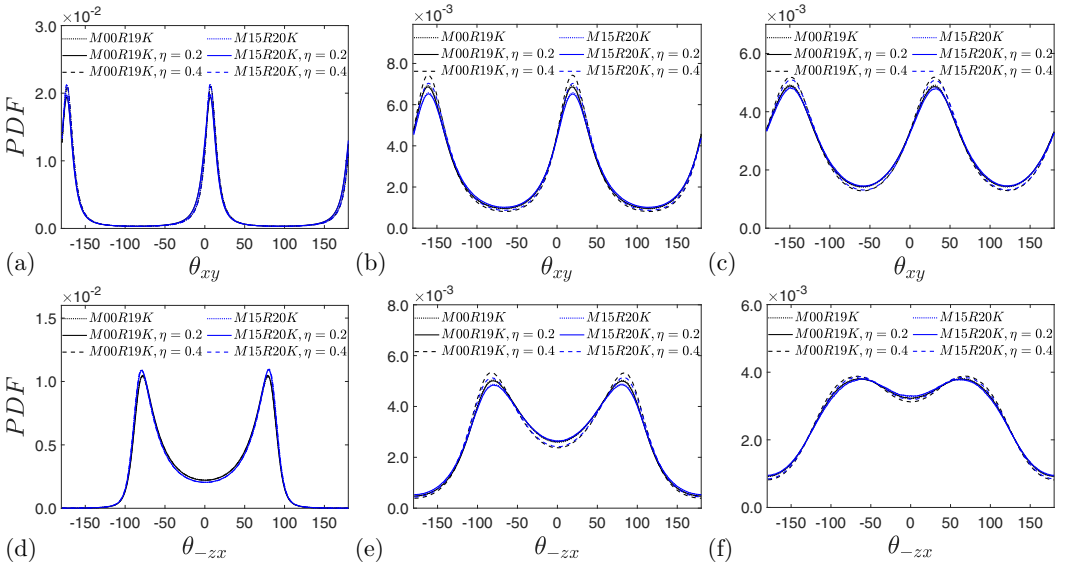

FIG. 24. PDFs of θ_{xy} and θ_{-zx} with different η using cases: M00R19K and M15R20K. The PDFs of θ_{xy} are plotted in the first row; θ_{-zx} in the second row. The first column presents the statistics at $y^+ \approx 15$, the second one $y^+ \approx 50$, and the third one $y^+ \approx 100$.

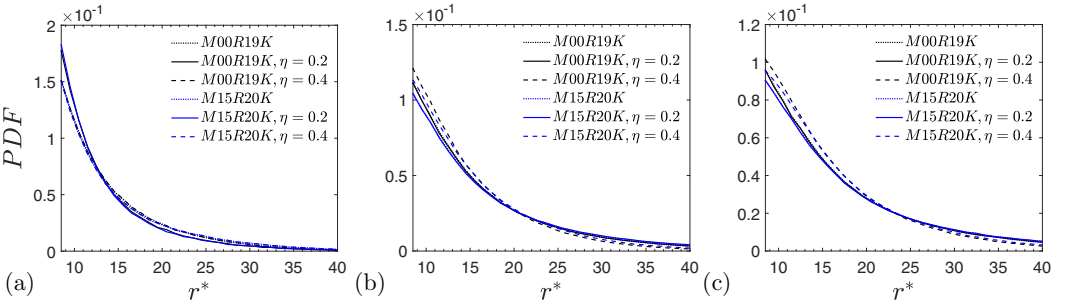

FIG. 25. PDFs of the vortex core radius r^* with different η using cases: M00R19K and M15R20K. The leftmost subfigure presents the statistics at $y^* \approx 15$, the middle one at $y^* \approx 50$, and the rightmost one at $y^* \approx 100$.

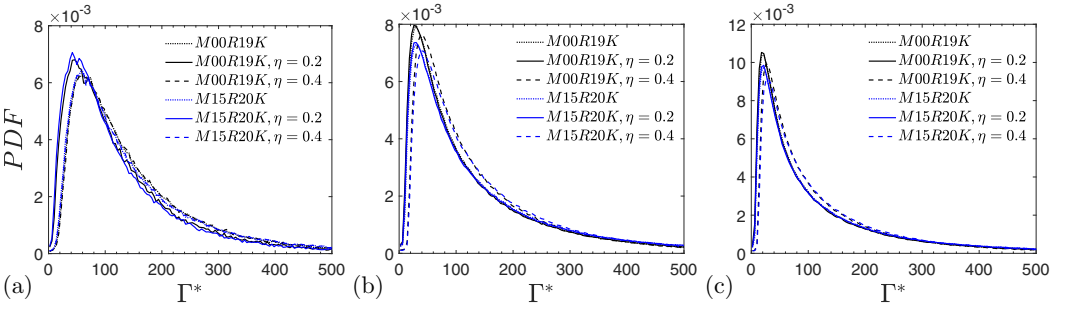

FIG. 26. PDFs of the vortex core circulation Γ^* with different η using cases: M00R19K and M15R20K. The leftmost subfigure presents the statistics at $y^* \approx 15$, the middle one at $y^* \approx 50$, and the rightmost one at $y^* \approx 100$.

[1] T. Theodorsen, Mechanism of turbulence, in *Proceedings of the 2nd Midwestern Conference on Fluid Mechanics* (Ohio State University, Columbus, Ohio, 1952), pp. 1–19.
[2] W. W. Willmarth and B. J. Tu, Structure of turbulence in the boundary layer near the wall, Phys. Fluids **10**, S134 (1967).
[3] G. R. Offen and S. J. Kline, A proposed model of the bursting process in turbulent boundary layers, J. Fluid Mech. **70**, 209 (1975).
[4] A. E. Perry and M. S. Chong, On the mechanism of wall turbulence, J. Fluid Mech. **119**, 173 (1982).
[5] S. K. Robinson, A perspective on coherent structures and conceptual models for turbulent boundary layer physics, in *AIAA Fluid Dynamics, 21st Plasma Dynamics and Lasers Conference* (AIAA, Reston, VA, 1990).
[6] C. R. Smith, J. D. A. Walker, A. H. Haidari, and U. Sobrun, On the dynamics of near-wall turbulence, Philos. Trans. R. Soc. Lond. A **336**, 131 (1991).
[7] S. J. Kline and S. K. Robinson, Quasi-coherent structures in the turbulent boundary layer. Part 1: Status report on a community-wide summary of the data, in *Near Wall Turbulence*, edited by S. J. Kline and N. H. Afgan (Hemisphere Publishing Corp., 1989), pp. 218–247.
[8] S. K. Robinson, Coherent motions in the turbulent boundary layer, Annu. Rev. Fluid Mech. **23**, 601 (1991).
[9] S. K. Robinson, The kinematics of turbulent boundary layer structure, Ph.D. thesis, Stanford University, 1991.
[10] J. D. A. Walker, The boundary layer due to rectilinear vortex, Proc. R. Soc. Lond. A **359**, 167 (1978).
[11] T. L. Doligalski and J. D. A. Walker, Shear layer breakdown due to vortex motion, in *Coherent Structure of Turbulent Boundary Layers*, edited by C. R. Smith and D. E. Abbott (Lehigh University, USA, 1978), p. 288.
[12] C. C. Chu and R. E. Falco, Vortex ring/viscous wall layer interaction model of the turbulence production process near walls, Exp. Fluids **6**, 305 (1988).
[13] C. R. Smith, J. D. A. Walker, A. H. Haidari, and B. K. Taylor, Hairpin vortices in turbulent boundary layers: The implications for reducing surface drag, in *Structure of Turbulence and Drag Reduction* (Springer, Berlin, 1990), pp. 51–58.
[14] M. S. Acarlar and C. R. Smith, A study of hairpin vortices in a laminar boundary layer. part 1. hairpin vortices generated by a hemisphere protuberance, J. Fluid Mech. **175**, 1 (1987).
[15] M. S. Acarlar and C. R. Smith, A study of hairpin vortices in a laminar boundary layer. part 2. hairpin vortices generated by fluid injection, J. Fluid Mech. **175**, 43 (1987).
[16] T. L. Hon and J. D. Walker, An analysis of the motion and effects of hairpin vortices, Tech. Rep. FM-11 (Department of Mechanical Engineering and Mechanics, Lehigh University, Bethlehem, PA, 1987).
[17] B. Green, *Fluid Vortices*, Vol. 30 (Springer Science & Business Media, New York, 1995).
[18] J. Carlier and M. Stanislas, Experimental study of eddy structures in a turbulent boundary layer using particle image velocimetry, J. Fluid Mech. **535**, 143 (2005).
[19] S. Pirozzoli, M. Bernardini, and F. Grasso, Characterization of coherent vortical structures in a supersonic turbulent boundary layer, J. Fluid Mech. **613**, 205 (2008).
[20] Q. Gao, C. Ortiz-Duenas, and E. K. Longmire, Analysis of vortex populations in turbulent wall-bounded flows, J. Fluid Mech. **678**, 87 (2011).
[21] C. Wang, Q. Gao, J. Wang, B. Wang, and C. Pan, Experimental study on dominant vortex structures in near-wall region of turbulent boundary layer based on tomographic particle image velocimetry, J. Fluid Mech. **874**, 426 (2019).
[22] Y. Wu and K. T. Christensen, Population trends of spanwise vortices in wall turbulence, J. Fluid Mech. **568**, 55 (2006).
[23] G. Elsinga, R. Adrian, B. Van Oudheusden, and F. Scarano, Three-dimensional vortex organization in a high-reynolds-number supersonic turbulent boundary layer, J. Fluid Mech. **644**, 35 (2010).
[24] L. Wang and X. Y. Lu, Statistical analysis of coherent vortical structures in a supersonic turbulent boundary layer, Chin. Phys. Lett. **28**, 034703 (2011).
[25] J. Yao and F. Hussain, Toward vortex identification based on local pressure-minimum criterion in compressible and variable density flows, J. Fluid Mech. **850**, 5 (2018).

[26] M. V. Morkovin, Effects of compressibility on turbulent flows, *Méchanique de la Turbulence* (Centre National de la Recherche Scientifique, Paris, 1962), p. 367.
[27] E. R. Van Driest, Turbulent boundary layer in compressible fluids, J. Aeronaut. Sci. **18**, 145 (1951).
[28] A. Trettel and J. Larsson, Mean velocity scaling for compressible wall turbulence with heat transfer, Phys. Fluids **28**, 026102 (2016).
[29] K. P. Griffin, L. Fu, and P. Moin, Velocity transformation for compressible wall-bounded turbulent flows with and without heat transfer, Proc. Natl. Acad. Sci. USA **118**, e2111144118 (2021).
[30] T. Bai, K. P. Griffin, and L. Fu, Compressible velocity transformations for various noncanonical wall-bounded turbulent flows, AIAA J. **60**, 4325 (2022).
[31] L. Fu, M. Karp, S. Bose, P. Moin, and J. Urzay, Shock-induced heating and transition to turbulence in a hypersonic boundary layer, J. Fluid Mech. **909**, A8 (2021).
[32] L. Fu, S. Bose, and P. Moin, Prediction of aerothermal characteristics of a generic hypersonic inlet flow, Theor. Comput. Fluid Dyn. **36**, 345 (2022).
[33] J. C. Del Alamo and J. Jiménez, Spectra of the very large anisotropic scales in turbulent channels, Phys. Fluids **15**, L41 (2003).
[34] J. C. Del Alamo, J. Jiménez, P. Zandonade, and R. D. Moser, Scaling of the energy spectra of turbulent channels, J. Fluid Mech. **500**, 135 (2004).
[35] J. C. Hunt, A. A. Wray, and P. Moin, Eddies, streams, and convergence zones in turbulent flows, Report No. 19890015184 (Center for Turbulence Research, Stanford University, 1988) (unpublished).
[36] J. Jeong and F. Hussain, On the identification of a vortex, J. Fluid Mech. **285**, 69 (1995).
[37] M. S. Chong, A. E. Perry, and B. J. Cantwell, A general classification of three-dimensional flow fields, Phys. Fluids **2**, 765 (1990).
[38] C. H. Berdahl and D. S. Thompson, Eduction of swirling structure using the velocity gradient tensor, AIAA J. **31**, 97 (1993).
[39] J. Zhou, R. J. Adrian, S. Balachandar, and T. Kendall, Mechanisms for generating coherent packets of hairpin vortices in channel flow, J. Fluid Mech. **387**, 353 (1999).
[40] B. Epps, Review of vortex identification methods, in *55th AIAA Aerospace Sciences Meeting* (AIAA, Reston, VA, 2017), p. 0989.
[41] C. Wang, Y. Shen, S. Mang, Q. Gao, Z. Wang, and J. Wang, A novel algorithm for visualizing and quantifying vortices in complex 3d flows based on marching and converging vortex atoms, Phys. Fluids **34**, 115131 (2022).
[42] D. C. Lay, S. R. Lay, and J. J. McDonald, *Linear Algebra and Its Applications* (Pearson, London, 2016).
[43] S. Robinson, Space-time correlation measurements in a compressible turbulent boundary layer, in *4th Joint Fluid Mechanics, Plasma Dynamics and Lasers Conference* (AIAA, Reston, VA, 1986), p. 1130.
[44] V. Kolár, Compressibility effect in vortex identification, AIAA J. **47**, 473 (2009).
[45] P. G. Huang, G. N. Coleman, and P. Bradshaw, Compressible turbulent channel flows: DNS results and modelling, J. Fluid Mech. **305**, 185 (1995).
[46] G. N. Coleman, J. Kim, and R. D. Moser, A numerical study of turbulent supersonic isothermal-wall channel flow, J. Fluid Mech. **305**, 159 (1995).
[47] A. Patel, B. J. Boersma, and R. Pecnik, The influence of near-wall density and viscosity gradients on turbulence in channel flows, J. Fluid Mech. **809**, 793 (2016).
[48] J. Zhou, Self-sustaining formation of packets of hairpin vortices in a turbulent wall layer, Ph.D. thesis, University of Illinois, Urbana-Champaign, 1997.
[49] B. Ganapathisubramani, E. K. Longmire, and I. Marusic, Experimental investigation of vortex properties in a turbulent boundary layer, Phys. Fluids **18**, 055105 (2006).
[50] X. Chen, C. Cheng, L. Fu, and J. Gan, Linear response analysis of supersonic turbulent channel flows with a large parameter space, J. Fluid Mech. **962**, A7 (2023).
[51] J. Jiménez and A. Pinelli, The autonomous cycle of near-wall turbulence, J. Fluid Mech. **389**, 335 (1999).
[52] M. J. Ringuette, M. Wu, and M. P. Martin, Coherent structures in direct numerical simulation of turbulent boundary layers at Mach 3, J. Fluid Mech. **594**, 59 (2008).
[53] R. J. Adrian, Hairpin vortex organization in wall turbulence, Phys. Fluids **19**, 041301 (2007).

[54] M. R. Head and P. Bandyopadhyay, New aspects of turbulent boundary-layer structure, J. Fluid Mech. **107**, 297 (1981).
[55] P. Moin and J. Kim, The structure of the vorticity field in turbulent channel flow. part 1. analysis of instantaneous fields and statistical correlations, J. Fluid Mech. **155**, 441 (1985).
[56] L. Wei and A. Pollard, Interactions among pressure, density, vorticity and their gradients in compressible turbulent channel flows, J. Fluid Mech. **673**, 1 (2011).
[57] J.-L. Balint, J. M. Wallace, and P. Vukoslavčević, The velocity and vorticity vector fields of a turbulent boundary layer. Part 2. Statistical properties, J. Fluid Mech. **228**, 53 (1991).
[58] M. Stanislas, L. Perret, and J. M. Foucaut, Vortical structures in the turbulent boundary layer: a possible route to a universal representation, J. Fluid Mech. **602**, 327 (2008).
[59] J. D. Anderson, *Modern Compressible Flow: With Historical Perspective* (McGraw–Hill, New York, 1990), Vol. 12.
[60] J. L. Ellzey, M. R. Henneke, J. M. Picone, and E. S. Oran, The interaction of a shock with a vortex: shock distortion and the production of acoustic waves, Phys. Fluids **7**, 172 (1995).
[61] L. Duan, I. Beekman, and M. Martin, Direct numerical simulation of hypersonic turbulent boundary layers. part 3. effect of mach number, J. Fluid Mech. **672**, 245 (2011).
[62] M. Cogo, F. Salvadore, F. Picano, and M. Bernardini, Direct numerical simulation of supersonic and hypersonic turbulent boundary layers at moderate-high reynolds numbers and isothermal wall condition, J. Fluid Mech. **945**, A30 (2022).
[63] J. Monty, N. Hutchins, H. Ng, I. Marusic, and M. Chong, A comparison of turbulent pipe, channel and boundary layer flows, J. Fluid Mech. **632**, 431 (2009).
[64] A. Perry, A. M. Uddin, and I. Marusic, An experimental and computational study on the orientation of attached eddies in turbulent boundary layers, in *Australasian Fluid Mechanics Conference* (1992), pp. 247–250.
[65] S. Gottlieb, C. W. Shu, and E. Tadmor, Strong stability-preserving high-order time discretization methods, SIAM Rev. **43**, 89 (2001).
[66] C. Cheng, W. Li, A. Lozano-Durán, and H. Liu, Identity of attached eddies in turbulent channel flows with bidimensional empirical mode decomposition, J. Fluid Mech. **870**, 1037 (2019).
[67] C. Cheng and L. Fu, Large-scale motions and self-similar structures in compressible turbulent channel flows, Phys. Rev. Fluids **7**, 114604 (2022).
[68] C. Cheng and L. Fu, Linear-model-based study of the coupling between velocity and temperature fields in compressible turbulent channel flows, J. Fluid Mech. **964**, A15 (2023).
[69] C. Cheng, W. Shyy, and L. Fu, Momentum and heat flux events in compressible turbulent channel flows, Phys. Rev. Fluids **8**, 094602 (2023).
[70] M. Lee and R. D. Moser, Direct numerical simulation of turbulent channel flow up to, J. Fluid Mech. **774**, 395 (2015).
[71] J. Yao and F. Hussain, Turbulence statistics and coherent structures in compressible channel flow, Phys. Rev. Fluids **5**, 084603 (2020).
[72] D. Modesti and S. Pirozzoli, Reynolds and mach number effects in compressible turbulent channel flow, Int. J. Heat Fluid Flow **59**, 33 (2016).